JAMES | Journal of Advances in Modeling Earth Systems

RESEARCH ARTICLE
10.1029/2024MS004467

The Land-Ocean Contrast in Deep Convective Intensity in a Global Storm-Resolving Model

Tristan H. Abbott[1,2], Nadir Jeevanjee[3], Kai-Yuan Cheng[1], Linjiong Zhou[1], and Lucas Harris[3]

[1]Cooperative Institute for Modeling Earth Systems, Princeton University, Princeton, NJ, USA, [2]Now at Breakthrough Energy, Kirkland, WA, USA, [3]NOAA/Geophysical Fluid Dynamics Laboratory, Princeton, NJ, USA

Key Points:

- Observations reveal a clear land-ocean contrast in the intensity of deep convection
- Only a subset of global storm-resolving models produce a comparably strong simulated land-ocean convective intensity contrast
- Existing theory does not capture drivers of a strong land-ocean convective intensity contrast simulated by a variant of the X-SHiELD model

Supporting Information:

Supporting Information may be found in the online version of this article.

Correspondence to:

N. Jeevanjee,
nadir.jeevanjee@noaa.gov

Citation:

Abbott, T. H., Jeevanjee, N., Cheng, K.-Y., Zhou, L., & Harris, L. (2025). The land-ocean contrast in deep convective intensity in a global storm-resolving model. *Journal of Advances in Modeling Earth Systems*, *17*, e2024MS004467. https://doi.org/10.1029/2024MS004467

Received 21 MAY 2024
Accepted 25 APR 2025

Abstract Observations reveal a clear difference in the intensity of deep convection over tropical land and ocean. This observed land-ocean contrast provides a natural benchmark for evaluating the fidelity of global storm-resolving models (GSRMs; global models with horizontal resolution on the order of kilometers), and GSRMs provide a potentially valuable tool for probing unresolved scientific questions about the origin of the observed land-ocean contrast. However, land-ocean differences in convective intensity have received relatively little attention in GSRM research. Here, we show that the strength of the land-ocean contrast simulated by GSRMs is strongly sensitive to details of GSRM implementations, and not clearly governed by any of several hypothesized drivers of the observed land-ocean contrast. We first examine DYAMOND Summer GSRM simulations, and show that only a subset produce a clear land-ocean contrast in the frequency of strong updrafts. We then show that the use of a sub-grid shallow convection scheme can determine whether or not the GSRM X-SHiELD produces a clear land-ocean contrast. Finally, we show that three putative drivers of the observed land-ocean contrast (convective available potential energy, boundary layer depth, and microphysics) fail to explain why a land-ocean contrast is present in X-SHiELD simulations with sub-grid shallow convection disabled. These results provide encouraging evidence that GSRMs can mimic the observed land-ocean convective intensity contrast. However, they also show that their ability to do so can be sensitive to uncertain sub-grid parameterizations, and suggest that existing theory may not fully capture drivers of the land-ocean contrast simulated by some GSRMs.

Plain Language Summary Observations, from satellites and aircraft, indicate that updrafts inside cumulonimbus clouds are significantly and systematically faster over land than over ocean. This observed "land-ocean contrast" is a valuable benchmark for global storm-resolving models (GSRMs), new computer models that are unique in their ability to simulate the entire atmosphere at a resolution high enough to model cumulonimbus clouds using the equations of fluid dynamics. GSRMs, in turn, provide a potentially valuable tool for testing explanations for why the land-ocean contrast exists in nature. This paper provides a foundation for using the observed land-ocean contrast as a benchmark for evaluating GSRMs by showing that GSRMs are capable of producing large land-ocean differences in the speeds of updrafts inside cumulonimbus clouds, but only if appropriate choices are made when setting up the model. Additionally, this paper provides a foundation for using GSRMs to test physical explanations for the land-ocean contrast by showing that three ideas from previous studies all fail to explain the strong land-ocean contrast simulated by one specific GSRM. These results highlight gaps in our ability to model and explain a striking feature of Earth's atmosphere, and encourage greater attention on the land-ocean contrast in future GSRM research.

1. Introduction

Satellite observations reveal a clear land-ocean contrast in proxies for the intensity of tropical deep convection. Lightning flash rates differ between land and ocean by more than an order of magnitude, and clearly highlight outlines of landmasses in multi-year climatologies (Cecil et al., 2014; Christian et al., 2003; E. Williams & Stanfill, 2002; E. J. Zipser et al., 2006, and see Figure 1a). Other satellite proxies for intense convection, including the frequency of overshooting convective tops, minimum microwave brightness temperatures, and echo top heights, show similarly stark land-ocean contrasts (e.g., Houze Jr et al., 2015; C. Liu et al., 2008; C. Liu & Zipser, 2015; C. Liu & Zipser, 2005; Nesbitt et al., 2006; E. Williams & Stanfill, 2002; E. J. Zipser et al., 2006).

The most parsimonious explanation for these striking satellite observations is that they are the observable manifestation of something more basic: a land-ocean contrast in convective updraft speeds. On physical grounds,

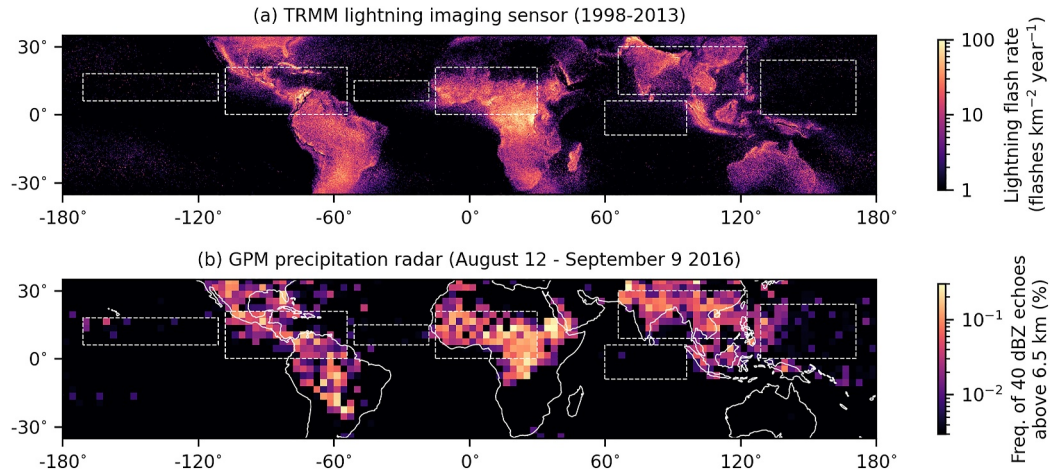

Figure 1. Mean lightning flash rate from the TRMM lightning imaging sensor (a) and frequency of 40 dBZ radar echoes above 6.5 km from the GPM precipitation radar (b). Panel (b) is based on along-track Ku-band reflectivity profiles from the GPM 2ADPR product between 12 August and 9 September 2016 (roughly the DYAMOND Summer analysis period), with frequencies computed by dividing the total number of observed pixels with a 40 dBZ echo above 6.5 km by the total number of observed pixels in 3°-by-3° latitude-longitude bins. Dashed lines show regions used to define the land-ocean contrast indices described in Section 2 and shown in Figure 2.

conditions for lightning generation by non-inductive charging—which requires frequent ice-ice collisions in the presence of supercooled water (T. Takahashi, 1978)—are more likely to occur in strong convective updrafts with vertical velocities above ∼7–10 m s^{-1} (Rutledge et al., 1992; E. R. Williams et al., 1992; E. J. Zipser & Lutz, 1994). Similarly, high maximum heights of high reflectivity—an effective proxy for lightning (e.g., Bang & Zipser, 2015; C. Liu et al., 2012)—are more likely when updrafts loft large hydrometeors high in the atmosphere. Moreover, in situ observations of convective updraft velocities contain striking differences between land and ocean. Early observations of cumulonimbus in Ohio and Florida include multiple aircraft penetrations of updrafts with vertical velocities of 15–20 m s^{-1} and a small number of observations of updraft velocities as high as 25 m s^{-1} (Table 7 of Byers and Braham (1949), Table 1 of Hallett et al. (1978)). Observations of vertical velocities over tropical oceans find comparatively much weaker updrafts: average vertical velocities for the strongest 10% of updrafts observed during GATE (Global Atmospheric Research Program Tropical Atlantic Experiment, LeMone and Zipser (1980); E. Zipser and LeMone (1980)), TAMEX (Taiwan Area Mesoscale Experiment, Jorgensen and LeMone (1989)), and EMEX (Equatorial Mesoscale Experiment, Webster and Houze Jr (1991)) were lower than those observed in Ohio and Florida during the Thunderstorm Project (Byers & Braham, 1949) by a factor of 2–3 (Figure 3 of Lucas, Zipser, & Lemone, 1994). More recent measurements of vertical velocity extremes document speeds as high as 50 m s^{-1} over land (Heymsfield et al., 2013; Musil et al., 1991) but only up to 20–25 m s^{-1} over ocean (Heymsfield et al., 2010; Lawson et al., 2015).

Neither physical arguments nor isolated observations are ironclad proof that differences in updraft speeds are responsible for land-ocean differences in satellite proxies for intense convection. Reflectivity and lightning flash rates are most directly linked to microphysical conditions within updrafts, which can be modulated independently of changes in vertical velocities by changes in aerosol concentrations that affect collision-coalescence, riming, and charge generation (A. C. Varble et al., 2023; E. Williams et al., 2002); and by changes in updraft width that affect condensate fallout (A. Varble et al., 2014). Nevertheless, the combination of satellite proxies, physical arguments, and observations of updraft speeds provide compelling evidence for a systematic land-ocean contrast in convective updraft velocities, which we refer to simply as the "land-ocean contrast" throughout this paper.

The observed land-ocean contrast presents a valuable but largely ignored test for global storm-resolving models (GSRMs). GSRM development is motivated, in part, by a hope that convection-permitting climate models will provide a breakthrough in our ability to model how weather, including extreme convective events, changes with climate (Ma et al., 2022; Palmer & Stevens, 2019; Stevens et al., 2019, 2020). Satellite proxies for strong updrafts show obvious land-ocean differences even on short time scales and in fields accessible to GSRMs: for example, a clear land-ocean contrast appears in the frequency of 40 dBZ echoes above 6.5 km observed during the month-

long DYAMOND Summer (Stevens et al., 2019) simulation period (Figure 1b). Confirming that GSRMs can reproduce observed differences between continental and oceanic convection would build confidence that GSRMs accurately capture controls on convective intensity. Matsui et al. (2016) took a step in this direction by assessing whether two models (one superparameterized model and one GSRM) captured land-ocean differences in reflectivity-based proxies for intense convection, and found that both struggled to reproduce observations. To our knowledge, however, no subsequent studies built on Matsui et al. (2016) by examining the land-ocean contrast in other GSRMs.

The observed land-ocean contrast also presents an opportunity for GSRMs, which seem uniquely well-suited to provide thus-far-elusive clarity on its physical drivers. A number of hypotheses exist, based on land-ocean differences in convective available potential energy (CAPE), boundary layer depth and updraft width, aerosol concentrations, and surface heterogeneity (Lucas, Zipser, & LeMone, 1994; Robinson et al., 2011; E. Williams & Stanfill, 2002; E. Williams et al., 2002; E. Zipser & LeMone, 1980). With the possible exception of CAPE (Hansen et al., 2020; Lucas, Zipser, & LeMone, 1994; Romps et al., 2018; H. Takahashi et al., 2023), these hypotheses are consistent with observations (Robinson et al., 2011; H. Takahashi et al., 2023; E. Williams & Stanfill, 2002). However, the inability of observations to provide counterfactual worlds without land-ocean differences in proposed drivers makes it difficult to test causality using observations alone.

Models, in contrast, can provide counterfactual worlds, and a number of previous studies have used limited-area cloud-resolving simulations to isolate and test causal drivers of the land-ocean differences in convective intensity. However, these efforts have not led to a clear consensus. Hansen et al. (2020) found that including a diurnal cycle in surface temperature had little effect on peak CAPE or updraft speeds in idealized cloud-resolving simulations. Mulholland et al. (2021) found that a deeper boundary layer produced wider, less dilute, and faster convective updrafts in short (30 min) initial-condition simulations, while Hansen and Back (2015) and Sarbeng (2023) found no increase in updraft speeds in response to increases in boundary layer depth in equilibrated radiative-convective equilibrium (RCE) simulations. Similarly, while Robinson et al. (2011) found that mesoscale variations in surface fluxes produced stronger updrafts in initial condition simulations, Sarbeng (2023) found that updraft speeds were insensitive to surface heterogeneity in RCE simulations.

Additionally, neither short-duration nor equilibrated limited-area simulations fully capture controls on environmental properties (e.g., clear-air temperature and humidity) that influence updraft buoyancy. In short-duration simulations, environmental properties are set primarily by prescribed initial conditions. In RCE simulations, updraft buoyancy is strongly constrained because environmental temperature profiles are determined by updraft temperatures (Abbott & Cronin, 2021; Seeley & Romps, 2016). This constraint can be relaxed by parameterizing large-scale circulations (Abbott & Cronin, 2021) or by running large-domain simulations with inhomogeneous boundary conditions (Hansen et al., 2020), but the former introduces uncertainty related to the large-scale dynamics parameterization, and the latter introduces uncertainty related to domain geometry. GSRMs, which explicitly simulate both small-scale convective dynamics and large-scale controls on environmental properties, provide a solution to this dilemma.

This paper, therefore, has two aims: first, to assess whether GSRMs produce clear land-ocean differences in the intensity of deep convection, with a particular focus on updraft velocities; and second, to leverage GSRM simulations to test hypotheses about the physical drivers of the land-ocean contrast. We focus primarily on the land-ocean contrast in simulations with eXperimental System for High-resolution prediction on Earth-to-Local Domains (X-SHiELD, Harris et al., 2020; Harris et al., 2021) developed at the Geophysical Fluid Dynamics Laboratory (GFDL), the authors' home institution. This approach allows us to experiment by running new simulations, rather than solely relying on existing model output. However, we first provide some context by using observations to calibrate our expectations for models, and by examining the distribution of intense updrafts across GSRMs in the DYAMOND Summer intercomparison (Stevens et al., 2019).

2. Calibrating Expectations for Models

Direct comparisons between the land-ocean contrast simulated in GSRMs and observed by satellites are difficult. GSRMs do not simulate lightning, and therefore provide no output that can be directly compared with observed lightning flash rates. It is possible in principle to compute reflectivity from GSRM outputs, and we initially assumed that this would be our basis for a model-observation comparison, similar to Matsui et al. (2016). In practice, however, we found simulated reflectivity to be strongly sensitive to microphysical parameters in one

GSRM (see Section 4 and Text S1 in Supporting Information S1), and in the process realized that the lack of realistic size sorting in single-moment microphysics schemes used by most GSRMs might prevent models from simulating a realistic relationship between reflectivity and vertical velocity. Together with similar results from previous kilometer-scale model intercomparisons (Fan et al., 2017; A. Varble et al., 2014), this led to concerns that microphysical details might obscure more fundamental inter-model differences in simulated updraft speeds. For these reasons, our evaluation of the land-ocean contrast in GSRM simulations focuses directly on simulated updraft speeds.

Because there are no global observations of convective updraft velocities, land-ocean differences in frequencies of strong updrafts cannot be compared directly to observed values. Instead, we use observations to calibrate our expectations for models by making the assumption that frequencies of strong updrafts (defined using suitable thresholds) are proportional to frequencies of satellite-observable proxies for strong updrafts. For simplicity, we use column-maximum vertical velocity as our metric of updraft intensity, since this avoids the need to develop and validate an algorithm for identifying updraft objects. We have no way to verify the validity of this proportionality assumption, or to exclude the possibility that a different measure of updraft intensity (e.g., mass flux or mean vertical velocity within an updraft object) may be more directly related to satellite-observable proxies, but view it as a reasonable null hypothesis absent evidence to the contrary.

We use two observational proxies for calibration: 1998–2013 average lightning flash rates from the TRMM Lightning Imaging Sensor Very High Resolution Climatology (Albrecht et al., 2016b) (Figure 1a), and frequencies of 40 dBZ echo tops above a threshold height in reflectivity profiles from the GPM satellite (Ku-band, 2ADPR product) during the DYAMOND Summer simulation period (e.g., Figure 1b). To enable a quantitative comparison between proxies and models, we define a land-ocean contrast index by constructing bounding boxes that delimit four regions of tropical ocean (roughly the western Pacific, eastern Pacific, Atlantic, and Indian oceans) and three regions of tropical land (the Americas, Africa, and Asia). The bounding boxes are shown as white dashed lines on Figure 1, and are designed to capture regions with frequent—but not necessarily intense—deep convection. Given a quantity of interest (e.g., lightning flash rates), we compute a representative oceanic value by (a) taking an area-weighted average over all oceanic grid cells within each of the four oceanic bounding boxes before (b) taking a simple average across the four tropical ocean regions. The simple average across ocean regions avoids assigning more weight to the larger western Pacific region than other smaller ocean regions. A representative land value is defined analogously based on averages over land grid cells within the three land bounding boxes. The ratio of the representative land and ocean values gives the land-ocean contrast index. We compute all land-ocean contrast indices using fields at 3° resolution, and define land and ocean grid cells as those with a land fraction above and below 10%, respectively.

1998–2013 average lightning flash rates produce a land-ocean contrast index of 32 (i.e., the representative land value is larger than the representative ocean value by a factor of 32) (Figure 2a, black point). The land-ocean contrast index derived from 40 dBZ echo top heights depends on the choice of threshold height. Because charge separation requires graupel and supercooled water in the mixed phase region, and high reflectivity provides an estimate of the height to which graupel is lofted, we expect to approximately reproduce the land-ocean contrast index for lightning with an appropriate height threshold somewhere within the mixed-phase region. Indeed, we find that a threshold height of 6.5 km produces a land-ocean contrast index of 29 (Figure 2a, large blue point), similar to the value derived from lightning flash rates. Picking a slightly lower threshold height (5.5 km) produces a lower land-ocean contrast index (7), and picking a higher threshold (7.5 km) produces a larger land-ocean contrast index (97) (Figure 2a, small blue points).

Based on these observational reference points, and subject to the assumption that frequencies of strong updrafts are proportional to frequencies of observable proxies, we feel that it is reasonable to expect models with a realistic land-ocean contrast to produce at least an order-of-magnitude land-ocean difference in the frequency of strong updrafts. We emphasize, again, that this expectation is not based on ironclad reasoning. Future observations (from e.g., the INCUS mission) may provide opportunities to update this expectation, and the underlying proportionality assumption could be tested using detailed regional modeling studies that leverage co-located measurements of satellite proxies and updraft velocities. Nevertheless, we feel that this expectation provides a useful guide, and proceed in the next section by examining whether we can find some definition of a "strong updraft" for which DYAMOND models produce an order-of-magnitude land-ocean contrast.

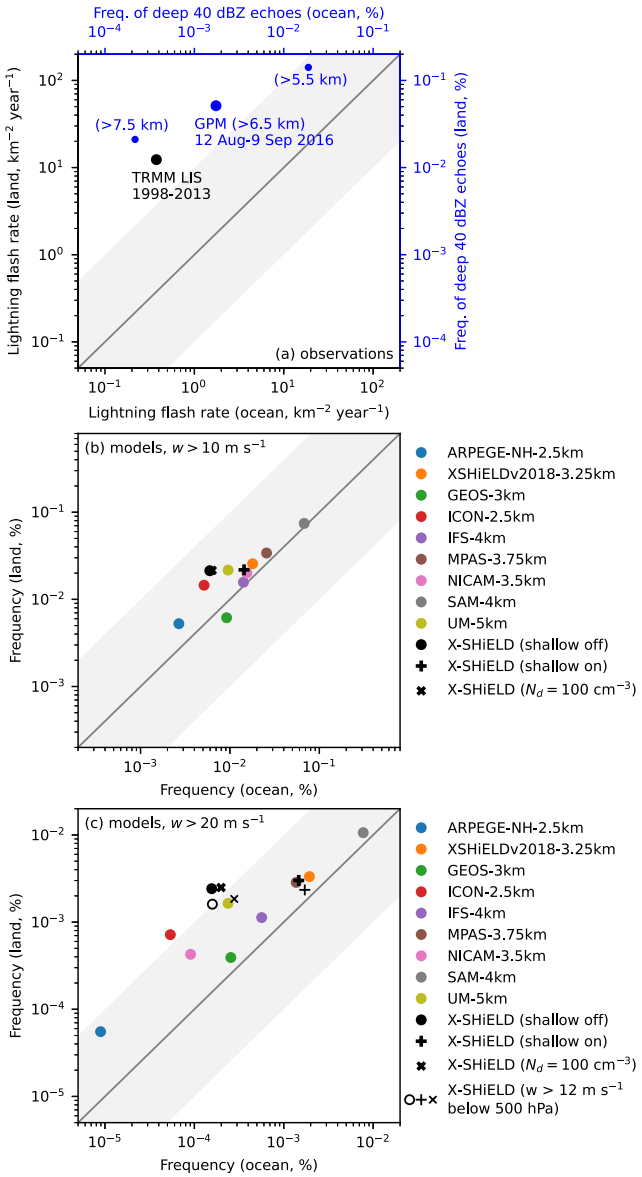

Figure 2. Land-ocean contrast indices for observed proxies for intense convective updrafts (a), simulated updrafts with vertical velocities above 10 m s^{-1} (b), and simulated updrafts with vertical velocities above 20 m s^{-1} (c). The vertical and horizontal axes show representative land and ocean values, respectively, and gray shading separates points corresponding to land-ocean contrast indices above and below 10. (Because axis scales are logarithmic, the land-ocean contrast index, i.e., the ratio of land to ocean frequencies, is simply the distance from the one-to-one line.) Indices for DYAMOND models (Section 3) are shown in colors, and indices for X-SHiELD simulations (Sections 4-5) are shown in black. In panel (c), black markers with light line weights show X-SHiELD indices for updrafts above 12 m s^{-1} below 500 hPa.

3. Land-Ocean Contrast in DYAMOND Simulations

We analyze the distribution of intense updrafts in DYAMOND Summer simulations contributed by 9 models: an early GFDL GSRM FV3 (nominal horizontal resolution of 3.25 km), ARPEGE-NH (2.5 km), GEOS (3 km), ICON (2.5 km), IFS (4 km), MPAS (3.75 km), NICAM (3.5 km), SAM (4 km), and UM (5 km). The earlier GFDL GSRM is called "FV3" in Stevens et al. (2019). However, we now recommend reserving usage of the name "FV3" to refer to the FV3 dynamical core (Putman & Lin, 2007) and not models. We will instead refer to the early GFDL GSRM as "X-SHiELD v2018" to distinguish it from the current version of X-SHiELD used later in this paper. Other abbreviations and acronyms follow Stevens et al. (2019), which also provides details about individual models. Each model ran a simulation from 1 August to 10 September 2016, initialized from the same meteorological analysis, and saved instantaneous 3D snapshots every 3 hr. The representation and initialization of land surface properties was not carefully controlled, and Stevens et al. (2019) provides only a brief description of the approaches taken by a subset of the ensemble.

For each model, we take 3D snapshots of vertical velocity fields on models' native grids, discard the first 10 days of each simulation as spin-up, and compute column-maximum vertical velocities from each remaining 3D snapshot. We then define 3°-by-3° latitude-longitude bins and compute the frequency with which column-maximum vertical velocities exceed a vertical velocity threshold within each bin. Absolute frequencies of strong updrafts vary widely between models, so in order to focus on relative differences between land and ocean we normalize frequencies by the 99th percentile frequency (a robust estimator of the maximum frequency), computed from values within 20° latitude of the equator. Finally, we plot normalized frequencies using a log-scale colormap that spans two orders of magnitude—the same range as colormaps that clearly show a land-ocean contrast in lightning flash rates and echo top heights (recall Figure 1)—and annotate plots with the normalization factor for converting absolute to relative frequencies.

Of the 9 models analyzed, none produce a land-ocean contrast in the frequency of 10 m s^{-1} updrafts that shows up clearly when plotted on a map using a two-order-of-magnitude log-scale colorbar (left column of Figure 3). Two models (ICON and UM) produce a reasonably clear land-ocean contrast in the frequency of 20 m s^{-1} updrafts, but other models (including X-SHiELD v2018) produce 20 m s^{-1} updrafts with comparable frequency over land and ocean (right column of Figure 3). Land-ocean contrast indices are consistent with these impressions: no DYAMOND model produces an order-of-magnitude land-ocean difference in the frequency of 10 m s^{-1}, and only ICON produces an order-of-magnitude difference in the frequency of 20 m s^{-1} updrafts, although UM comes close (Figures 2b and 2c). Even for ICON, the fact that an order-of-magnitude difference appears only for 20 m s^{-1} updrafts is an important caveat on the realism of the results, since this is much faster than the minimum vertical velocity required to produce lightning (Rutledge et al., 1992; E. R. Williams et al., 1992; E. J. Zipser & Lutz, 1994).

The considerable diversity amongst DYAMOND models suggests that the presence of a realistic land-ocean contrast in convective intensity is not a ubiquitous feature of GSRM simulations, and instead depends on choices made during model development. This inference is supported by additional X-SHiELD experiments run during the DYAMOND Summer period, which we describe in the next section.

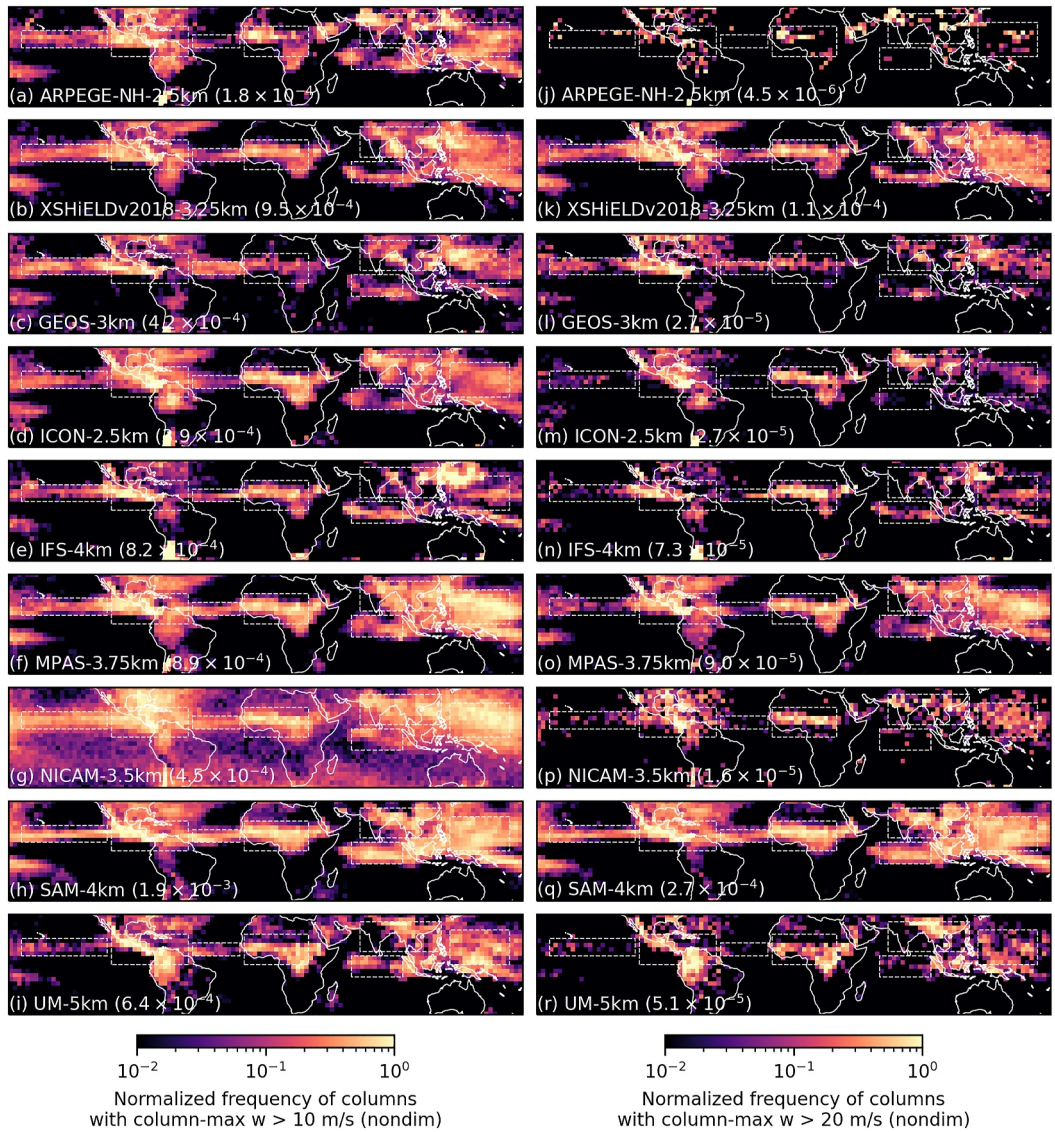

Figure 3. Normalized frequency of column-maximum updraft velocities above 10 m s^{-1} (a–i) and 20 m s^{-1} (j–r) in DYAMOND Summer simulations. Labels in the bottom right of each panel include the nominal model resolution and frequency normalization factor. The normalization factor is dimensionless (i.e., it is a fraction, not a percent). Note that the normalizing frequencies, which provide a measure of the absolute frequency of strong updrafts, vary by more than a factor of 10 with a threshold of 10 m s^{-1} and almost a factor of 100 (ignoring ARPEGE) with a threshold of 20 m s^{-1}. Dashed lines show regions used to define the land-ocean contrast indices described in Section 2 and shown in Figure 2.

4. Land-Ocean Contrast in X-SHiELD

X-SHiELD is a GSRM that uses a finite-volume cubed-sphere dynamical core (Harris et al., 2020, 2021; Putman & Lin, 2007) with ∼3.25 km horizontal resolution and 79 vertical levels, and is coupled to a mixed-layer ocean model (Pollard et al., 1973) with sea surface temperature nudged toward ECMWF analyses with a 15 days time scale. In its default configuration, X-SHiELD is run with sub-grid parameterizations for microphysics (the GFDL in-line microphysics scheme, Harris et al., 2020; Zhou et al., 2022), boundary layer turbulence (a turbulence-kinetic-energy-based eddy-diffusivity mass-flux scheme, Han & Bretherton, 2019), land surface processes (the NOAH land surface scheme, Ek et al., 2003), and shallow convection (a scale-aware simplified Arakawa-Schubert scheme, Han et al., 2017) but not deep convection. Surface topography data are taken from the United States Geological Survey Global Multi-Resolution Terrain Data (30 arcsecond resolution, Danielson &

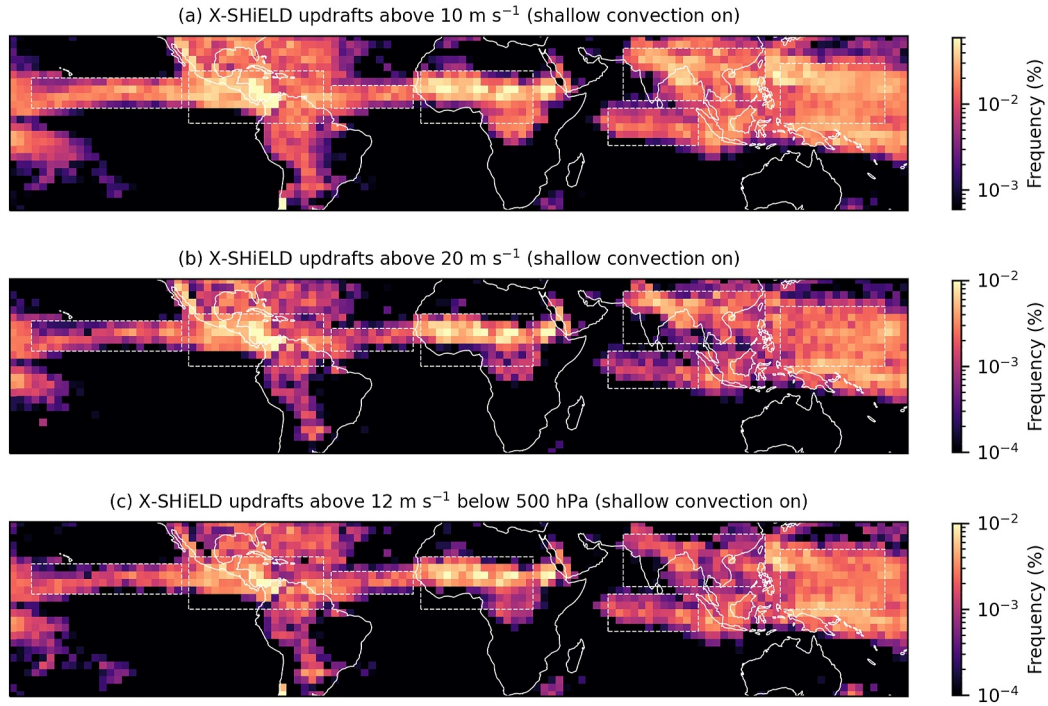

Figure 4. Frequency of column-maximum updraft velocities above 10 m s^{-1} (a) and 20 m s^{-1} (b), and frequency of updraft velocities above 12 m s^{-1} between the surface and 500 hPa (c), in X-SHiELD with parameterized shallow convection enabled. Dashed lines show regions used to define the land-ocean contrast indices described in Section 2 and shown in Figure 2.

Gesch, 2011) and albedo climatologies are from MODIS (Barlage et al., 2005; Gao et al., 2005; Schaaf et al., 2002).

Whether X-SHiELD produces a clear land-ocean contrast in convective intensity turns out to be strikingly sensitive to whether it is run with parameterized shallow convection. To show this, we compare two X-SHiELD simulations: one using the model's default configuration, and a second with the shallow convection scheme disabled. Both simulations are initialized from an Integrated Forecasting System analysis at the beginning of the DYAMOND Summer simulation period (1 August 2016) and allowed to run freely until 9 September 2016 with 3D snapshots saved every 3 hr. We analyze land-ocean differences in updraft speeds using the same methods as our analysis of the DYAMOND ensemble, with two differences. First, we also compute the frequency with which vertical velocities exceed 12 m s^{-1} between the surface and 500 hPa. This statistic captures updraft speeds below and in the mixed-phase region of tropical deep convective clouds, which may have a closer relationship to storm electrification than column-maximum updraft speed (E. J. Zipser & Lutz, 1994). Second, because we no longer have to deal with a large ensemble of models with large inter-model differences in the absolute frequencies of strong updrafts, we plot frequencies for X-SHiELD simulations without normalization.

When run with default subgrid parameterizations, X-SHiELD produces similar land and ocean frequencies of 10 m s^{-1} updrafts, 20 m s^{-1} updrafts, and 12 m s^{-1} updrafts below 500 hPa (Figure 4). Land-ocean contrast indices are well below a factor of 10 for all three thresholds (Figures 2b and 2c). Using other vertical velocity thresholds produces similar results. In other words, like X-SHiELD v2018, current X-SHiELD with default physical parameterizations does not produce a clear land-ocean contrast in the frequency of strong updrafts, and this conclusion does not depend on the details of how "strong updrafts" are defined.

In contrast, X-SHiELD does produce a clear land-ocean contrast when run with the shallow convection scheme disabled. Land-ocean differences in the frequency of 20 m s^{-1} updrafts and in the frequency of 12 m s^{-1} updrafts below 500 hPa appear clearly when plotted with a two-order-of-magnitude log-scale colormap (Figures 5b and 5c), similar to observed proxies for intense convection. Land-ocean contrast indices for both 20 m s^{-1} updrafts and 12 m s^{-1} updrafts below 500 hPa are a factor of 10 or larger (Figure 2c), consistent with calibrated expectations for

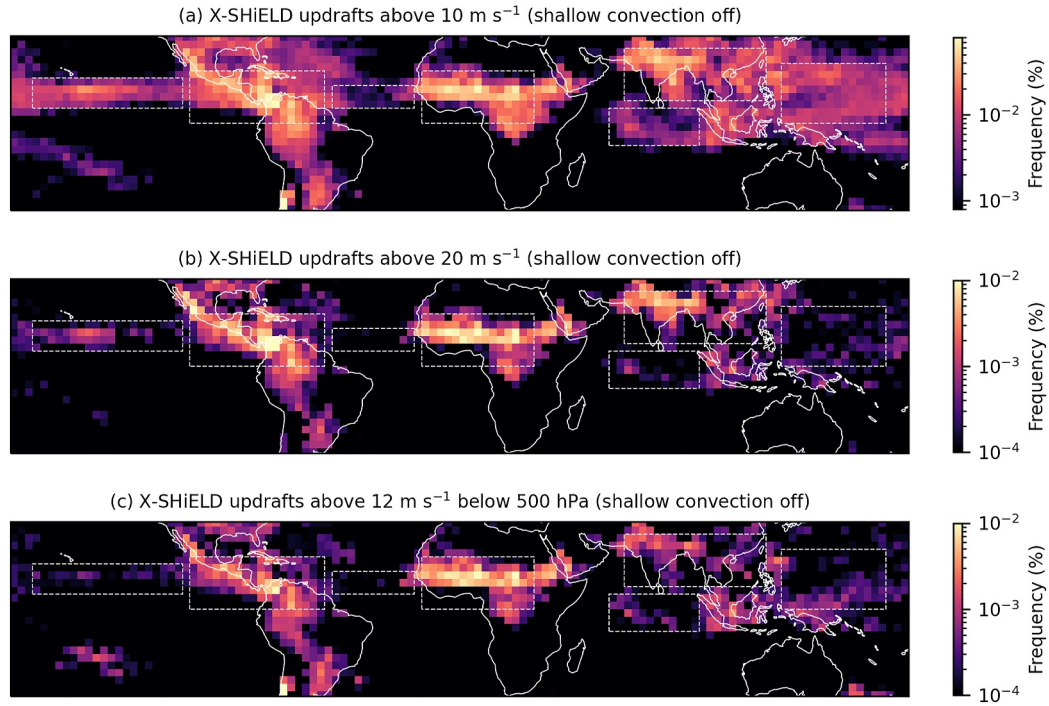

Figure 5. Frequency of column-maximum updraft velocities above 10 m s^{-1} (a) and 20 m s^{-1} (b), and frequency of updraft velocities above 12 m s^{-1} between the surface and 500 hPa (c), in X-SHiELD with parameterized shallow convection disabled. Dashed lines show regions used to define the land-ocean contrast indices described in Section 2 and shown in Figure 2.

models with a realistic land-ocean contrast (Section 2). The dramatic increase in the strength of the land-ocean contrast, relative to the simulation with an active shallow convection scheme, is caused primarily by a reduction in the frequency of strong updrafts over ocean, and not by an increase in the frequency of strong updrafts over land. Detecting the land-ocean contrast requires a sufficiently restrictive definition of "strong updraft": for example, the land-ocean contrast in the frequency of 10 m s^{-1} updrafts (without masking based on pressure levels) remains weak (Figure 5a), and the corresponding land-ocean contrast index is well below 10 (Figure 2b). 20 m s^{-1} is the lowest vertical velocity threshold that produces a clear land-ocean contrast in column-maximum updraft speeds, and 12 m s^{-1} is the lowest vertical velocity threshold that produces a clear land-ocean contrast in updraft speeds between the surface and 500 hPa. Like the ICON DYAMOND simulation, X-SHiELD with shallow convection disabled produces a clear land-ocean contrast only when using vertical velocity thresholds above the $\sim$7 m s^{-1} updraft speed required to produce lightning in nature. Excluding simulated updrafts above the mixed-phase region reduces but does not eliminate this discrepancy.

Because strong convective updrafts can loft large hydrometeors high in the atmosphere, large reflectivities high in the atmosphere are frequently used as proxies for strong convective updrafts in observations (e.g., Houze Jr et al., 2015; C. Liu & Zipser, 2005; C. Liu & Zipser, 2015; C. Liu et al., 2008; Nesbitt et al., 2006; E. Williams & Stanfill, 2002; E. J. Zipser & Lutz, 1994; E. J. Zipser et al., 2006). In X-SHiELD, however, land-ocean differences in the frequency of large simulated reflectivities high in the atmosphere bear surprisingly little resemblance to land-ocean differences in the frequency of strong updrafts. We provide details in Text S1 of Supporting Information S1. In brief, simulations with parameterized shallow convection enabled and disabled both fail to produce clear land-ocean differences in the frequency of reflectivity-based proxies for intense convection, even though the simulation with parameterized shallow convection disabled produces a vastly stronger land-ocean contrast in the frequency of strong updrafts (Figures S1 and S2 in Supporting Information S1). Increasing hydrometeor terminal fall speeds can produce a stronger relationship between the frequency of strong updrafts and large simulated reflectivity values high in the atmosphere (Figures S3 and S4 in Supporting Information S1), suggesting that microphysical biases (e.g., an underestimation of the fall speeds of very large hydrometeors in X-SHiELD's single-moment microphysics scheme) may limit X-SHiELD's ability to reproduce observed land-ocean

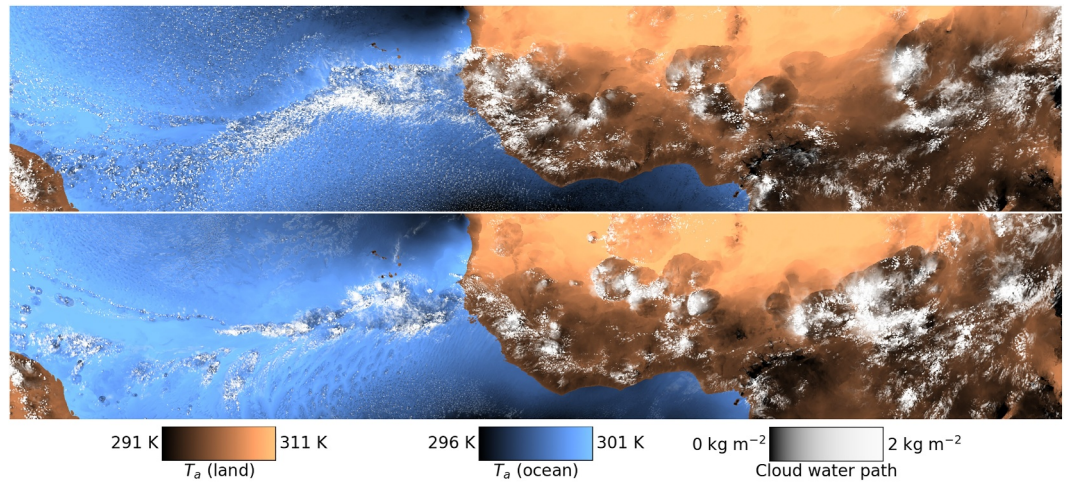

Figure 6. Snapshots of near-surface air temperature and cloud water path (liquid + ice) in X-SHiELD simulations with parameterized shallow convection disabled (top) and enabled (bottom) at 21Z on 11 August 2016. Full-resolution images with one pixel per model grid cell are available as supplementary data.

differences in reflectivity-based proxies for intense convection. However, biases in the simulated updraft velocity spectrum may also play a role. Comparing the frequency of intense updrafts with the frequency of thunder recorded by ground stations suggests that, even with parameterized shallow convection disabled, the simulated land-ocean contrast may be confined to somewhat more extreme (i.e., less frequent) events than the observed land-ocean contrast (Text S2 and Figure S6 in Supporting Information S1).

The first of this paper's two aims is to assess whether GSRMs produce clear land-ocean differences in the intensity of deep convection. Our analysis of the DYAMOND Summer ensemble and of X-SHiELD simulations suggests that GSRMs *can* produce substantial land-ocean differences in convective intensity, but do not do so automatically. Some, but not all, DYAMOND Summer simulations produce a clear land-ocean difference in the frequency of strong updrafts. X-SHiELD does not produce a clear land-ocean contrast in updraft speeds with default sub-grid parameterizations, but does when parameterized shallow convection is disabled.

Why certain models and model configurations produce much stronger land-ocean contrasts than other remains an open question, and is beyond the scope of this paper. ICON, UM, and X-SHiELD do not, to the best of our knowledge, share any parameterizations or infrastructure, and are based on dynamical cores with very different numerical schemes (Putman & Lin, 2007; Wood et al., 2014; Zängl et al., 2015). Parameterized shallow convection does not appear to be an inherent obstacle to simulating a strong land-ocean contrast, nor does disabling parameterized shallow convection guarantee a strong land-ocean contrast: UM's DYAMOND simulation ran with parameterized shallow convection (Stevens et al., 2019) and produced a fairly strong land-ocean contrast and, while SAM's ran without parameterized shallow convection (Stevens et al., 2019) and produced a weak land-ocean contrast.

For X-SHiELD specifically, a number of exploratory analyses failed to produce a clear explanation for the effect of parameterized shallow convection on the land-ocean contrast. We compared daily maximum CAPE values in X-SHiELD simulations with parameterized shallow convection enabled and disabled and did not find consistent changes that could explain the widespread changes in the frequency of strong oceanic updrafts (Figure S7 in Supporting Information S1). We also compared mean relative humidity profiles in the two simulations to see whether a reduction in mid-level relative humidity could be increasing updraft dilution over ocean in the simulation with parameterized shallow convection disabled, but instead found an increase in mid-level relative humidity over oceans (Figure S8 in Supporting Information S1). One striking change in the simulation with parameterized shallow convection disabled is an apparent decrease in the strength of convective organization over ocean. This change, which is widespread across ocean basins, is illustrated in a snapshot of the Sahel and Atlantic ITCZ (Figure 6). In the simulation with parameterized shallow convection disabled, oceanic convection is scattered, and there are only a few regions in the Atlantic ITCZ where convection is completely suppressed. In the simulation with parameterized convection enabled, there are broad regions in the Atlantic ITCZ where convection

is inactive, and active convection occupies relatively localized clusters. Though we do not show this conclusively, it possible that weaker organization of oceanic convection leads to an increase in updraft dilution—independent of changes in mean relative humidity—when parameterized convection is disabled.

The second of this paper's two aims is to leverage GSRM simulations to test hypotheses about the physical drivers of the land-ocean contrast. We feel that the X-SHiELD simulation with parameterized shallow convection disabled provides our best opportunity to pursue this goal. Although the land-ocean contrast in this simulation compares imperfectly with observations, this simulation does produce clear land-ocean differences in simulated updraft speeds, and probing underlying drivers is likely to provide some insight into the minimal physics required to generate a land-ocean contrast in convective intensity. This is the focus of the remainder of the paper.

5. Drivers of the Land-Ocean Contrast in X-SHiELD

When run with parameterized shallow convection disabled, X-SHiELD produces clear land-ocean differences in the frequency of strong convective updrafts. In this section, we probe the minimal physics required to produce this simulated land-ocean contrast by asking whether three hypothesized drivers of the observed land-ocean contrast —land-ocean differences in CAPE, updraft width, and microphysics—are necessary preconditions for the land-ocean contrast simulated by X-SHiELD. Note that this section focuses exclusively on the X-SHiELD simulation with parameterized shallow convection disabled, as this is the configuration that produces a land-ocean contrast in convective intensity. We emphasize that results in this section provide direct insight into drivers of the land-ocean contrast in X-SHiELD, and any implications for drivers of the land-ocean contrast in nature are suggestive rather than conclusive. We cannot exclude the possibility that X-SHiELD is producing a land-ocean contrast for the wrong reasons, so evidence that a particular hypothesized driver is not part of the minimal physics required to produce a land-ocean contrast in X-SHiELD does not necessarily imply that it plays no role in nature.

5.1. CAPE

There are intuitive reasons to expect peak CAPE to be higher over tropical land than tropical ocean. The low thermal inertia of land relative to ocean produces a much larger diurnal cycle of surface temperature and surface enthalpy fluxes, and recent work suggests that spatial variations in surface wetness may generate capping inversions that promote the buildup of high CAPE values (Emanuel, 2023; Tuckman et al., 2023).

However, a number of studies cast doubt on whether land-ocean differences in peak CAPE are an essential driver of observed land-ocean differences in convective intensity. Romps et al. (2014) developed a simple CAPE-based proxy for lightning that captures spatial and temporal variations in lightning flash rates over the continental US, but Romps et al. (2018) subsequently showed that this proxy does not capture land-ocean differences in lightning flash rates. Hansen et al. (2020) showed that high-percentile CAPE computed from ERA-Interim reanalysis is similar over tropical land and ocean, and argued based on limited-area cloud-resolving model simulations that convection prevents the buildup of high CAPE over land by generating sinks of boundary layer moist static energy that balance sources from surface enthalpy fluxes even on sub-diurnal time scales. H. Takahashi et al. (2023) analyzed CAPE computed from ECMWF operational analyses, co-located with deep convective cores identified in satellite data, and concluded that neither CAPE nor the shape of undilute buoyancy profiles could explain the land-ocean convective intensity contrast. These studies share a potential weakness in that they rely on CAPE from analyzed fields, which may underestimate true peak CAPE values (Wang et al., 2021), but nevertheless suggest that the observed land-ocean contrast is not driven by land-ocean differences in CAPE.

Our X-SHiELD simulation provides an opportunity to compare land-ocean differences in updraft speeds with land-ocean differences in CAPE within a single simulation, and so avoids potential pitfalls associated with comparing directly observed proxies for convective intensity with CAPE from analyzed atmospheric fields. We compute CAPE from 3-hourly instantaneous fields on the X-SHiELD native grid by lifting parcels from the lowest model level along pseudoadiabats. We include ice in CAPE calculations by assuming that the fraction of supercooled condensate varies linearly with temperature from 1 at 0°C to 0 at −40°C, and compute CAPE from virtual temperature profiles by integrating over regions of positive parcel buoyancy. We use the same procedure for calculating lifted parcel temperature profiles over land and ocean, which means that any land-ocean differences in CAPE must be produced by land-ocean differences in environmental temperature profiles or thermodynamic properties of air in the lowest model level.

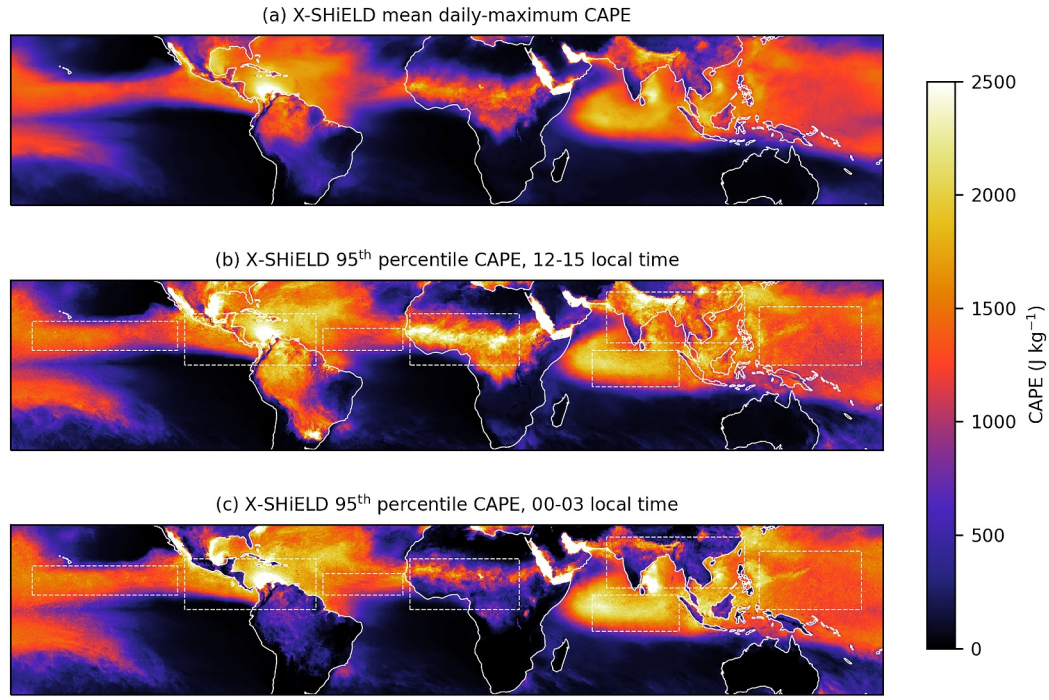

Figure 7. Average daily maximum CAPE (a) and 95th percentile CAPE between 12 and 3p.m. local time (b) and 12 and 3a.m. local time (c) in X-SHiELD with parameterized shallow convection disabled. Dashed lines show regions used to produce Figure 8.

We first plot daily maximum CAPE, a simple proxy for peak pre-convective CAPE, averaged across each day of the simulation (Figure 7a). Mean daily maximum CAPE does not show clear evidence for elevated values over land relative to ocean. Some land regions (e.g., the Sahel and the Indian subcontinent) have mean daily maximum CAPE values comparable to oceans, but other (e.g., Southeast Asia and Central America) have mean daily maximum CAPE values lower than oceans.

To understand why daily maximum CAPE is not higher over land despite the presence of a large diurnal cycle in surface temperature and surface fluxes, we compute diurnally resolved high-percentile CAPE as follows. At each grid point, we bin CAPE values by the local time of day, using 8 three-hour-wide bins. We approximate local solar time for each grid point by adding the Greenwich hour angle corresponding to the longitude of the grid point to the current Coordinated Universal Time. We then compute CAPE quantiles for each time bin at each model grid point.

Ninety-fifth percentile early afternoon CAPE (Figure 7b) does not show clear systematic differences between land and ocean. Although certain land regions (e.g., the Sahel) stand out as regions with unusually high afternoon CAPE, no CAPE threshold clearly separates regions of tropical land with frequent strong updrafts from regions of tropical ocean where strong updrafts are rare. There is a clear difference between 95th percentile land and ocean CAPE at nighttime (Figure 7c), but only because overnight CAPE is systematically *lower* over land than over ocean. This suggests that a strong diurnal cycle does not increase daily maximum CAPE over land relative to ocean because the diurnal cycle is accommodated by decreasing CAPE at night rather than increasing CAPE during the day.

Accommodation of the diurnal cycle through nighttime decreases in CAPE can be seen more clearly by averaging values displayed in Figures 7b and 7c over tropical land and ocean regions used to defined land-ocean contrast indices. For each 3 hr local time bin, we take 95th percentile CAPE values across all grid points with the land and (separately) ocean regions. This provides single representative values for 95th percentile CAPE, as a function of time of day, over tropical land and tropical ocean (Figure 8a). Representative values over ocean are around 1,500 J kg^{-1} regardless of time of day. Representative values over tropical land vary with the time of day, with a minimum around 500 J kg^{-1} in the early morning and a maximum around 1,600 J kg^{-1} during the early afternoon.

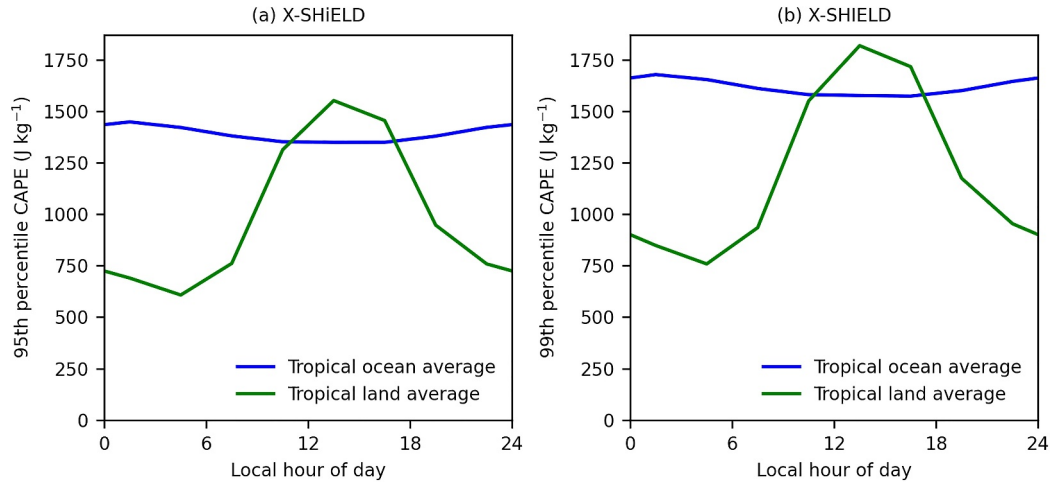

Figure 8. 95th (a) and 99th (b) percentile CAPE, computed as a function of location and local time as shown in Figure 7, then averaged in space over land and ocean inside the tropical land and ocean regions defined in Section 2 and shown in thin dashed line in Figure 7.

Consistent with CAPE maps, there is little difference between peak CAPE in deep convective regions over tropical land and ocean, and there is no time of day when land CAPE is significantly higher than ocean CAPE. This conclusion remains the same if we repeat this analysis for higher CAPE percentiles: 99th percentile CAPE values, for example, are also similar over land and ocean during the early afternoon (Figure 8b).

These results suggest that land-ocean differences in peak CAPE are *not* necessary to produce the land-ocean contrast in updraft speeds simulated by X-SHiELD. Some caveats apply: CAPE has more than one definition, and it is possible that a different CAPE variant—for example, CAPE based on reversible adiabatic ascent, or mixed-layer CAPE—is both more closely related to simulated updraft speeds and varies more between land and ocean. As pointed out by E. J. Zipser (2003), CAPE may provide relatively little insight into the behavior of convection without accounting for entrainment, condensate loading, and the vertical distribution of parcel buoyancy; metrics such as entraining CAPE (which incorporates parcel dilution; Peters, Chavas, et al., 2023) or the lifted index or normalized CAPE (which are sensitive to the shape of undilute buoyancy profiles; Blanchard, 1998; Galway, 1956) could potentially provide a better foundation for studying land-ocean differences in convective intensity. At the same time, our results are physically sensible given basic expectations for tropical convection based on quasi-equilibrium (Arakawa & Schubert, 1974; Emanuel, 2007) and weak temperature gradient (Charney, 1947; Sobel & Bretherton, 2000) theory. In the limit of strict quasi-equilibrium and zero free-tropospheric temperature gradients, convecting regions in the tropics must have the same sub-cloud moist static energy and free-tropospheric temperatures, and therefore the same CAPE, regardless whether convection occurs over land or ocean (Zhang & Fueglistaler, 2020). While real-world subcloud moist static energy and free-tropospheric temperatures include fluctuations around mean values, and basic theory does not require fluctuations to produce the same CAPE extremes over land and ocean, these fluctuations do not appear to produce a strong land-ocean contrast in peak CAPE in X-SHiELD.

5.2. Updraft Width

An alternative hypothesized driver of the observed land-ocean convective intensity contrast is that land-ocean differences in boundary layer properties produce convective updrafts that are wider and less strongly diluted by entrainment over land (Lucas, Zipser, & Lemone, 1994; E. Williams & Stanfill, 2002; E. J. Zipser, 2003). Larger boundary layer depths produced by lower surface wetness over land are often invoked as the key difference between the continental and oceanic boundary layer (Hansen & Back, 2015; Lucas, Zipser, & LeMone, 1994; Mulholland et al., 2021; H. Takahashi et al., 2023; E. Williams & Stanfill, 2002; E. Williams et al., 2005; E. J. Zipser, 2003), though land-ocean differences in updraft morphology could also arise from land-ocean differences in mesoscale convergence associated with surface heterogeneity (S. Liu et al., 2023) or from differences in the depth and strength of cold pools (Drager et al., 2020). This hypothesis is consistent with observations of updraft

widths. Data from aircraft penetrations provides some evidence that typical convective updrafts are several hundred meters wide over tropical oceans but can be several kilometers wide over land (Lucas, Zipser, & Lemone, 1994; E. Williams & Stanfill, 2002; E. J. Zipser, 2003). Additionally, satellite data shows evidence for lower entrainment rates in wider deep convective cores (H. Takahashi et al., 2021), as well as evidence for a systematic difference in the width of deep convective cores over land and ocean (H. Takahashi et al., 2023).

Evidence for a systematic difference in updraft widths over land and ocean in our X-SHiELD simulation would also be consistent with the hypothesis that land-ocean differences in updraft width drive the observed land-ocean contrast in convective intensity. However, we instead find that the coarse resolution of the X-SHiELD simulation (relative to the width of convective updrafts in nature) produces updrafts that are locked to the grid scale, with at most minor differences over land and ocean. In other words, we find that X-SHiELD inadvertently produces a mechanism denial experiment without a realistic land-ocean difference in updraft width, and the presence of a land-ocean contrast in the frequency of strong updrafts indicates that the simulated land-ocean contrast in convective intensity is not driven by land-ocean differences in updraft width.

To demonstrate that X-SHiELD produces grid-locked updrafts with similar widths over land and ocean, we construct a database of simulated updrafts identified in 3 hourly snapshots of fields on the X-SHiELD native grid. Our updraft identification algorithm focuses on low-level updrafts, in part because the hypothesized link between boundary layer depth and updraft width suggests that land-ocean differences in updraft widths should be apparent in nascent updrafts emerging from the top of the boundary layer, and in part because the relevant causal link is between updraft widths at lower levels and updraft speeds at higher levels. We first interpolate vertical velocity and cloud water mass fraction to the level where $\sigma = p/p_s = 0.8$, where p is pressure and p_s is surface pressure. We then identify updrafts as contiguous regions on the $\sigma = 0.8$ level (using 4-component connectivity) with vertical velocity above 1 m s^{-1} and cloud water mass fraction above 10^{-5} kg kg^{-1}. Grid cells nears the edges of faces in the X-SHiELD cubed sphere grid are handled by padding fields with values from neighboring faces. The width of the padding is 64 grid cells, which is large compared to typical updraft widths. We compute the area of each updraft by summing the areas of all grid cells inside the updraft, and them compute updraft widths as the square root of updraft areas. Finally, we discard all updrafts that are outside of the tropical land and ocean regions defined in Section 2.

In some cases, this procedure identifies elongated features on the edges of convective cold pools that, although typically only a few grid cells wide, can be hundreds of grid cells long. This is most common over land where vigorous convective cold pools produce strong local lifting along gust fronts. To quantify the impact these features have on our results, we compare results based on all identified updrafts with results where elongated features are filtered out by keeping only updrafts with convex cross-sections. Figure S9 in Supporting Information S1 shows the locations of all identified updrafts, with and without filtering for convex cross-sections.

Updraft width distributions show no evidence of a clear separation between land and ocean (Figure 9), regardless whether the distributions include all updrafts or only updrafts with convex cross-sections. Almost all updrafts are between 1 and 3 grid cells wide (widths of ∼3.25–9.75 km), suggesting that updraft widths are constrained by model resolution, as expected in a kilometer-scale model (Jeevanjee, 2017). Shapes of updraft width distributions are nearly identical over land and ocean, and land- and ocean-average updraft widths differ by only a few tenths of a kilometer, much less than the model grid spacing. The right tail of the updraft width distributions is thicker over land than over ocean, indicating that the very widest updrafts are somewhat more frequent over land. However, differences in simulated width distributions are minor compared to differences in width distributions documented in observations (H. Takahashi et al., 2023; E. Williams & Stanfill, 2002).

An additional analysis of the morphology of 3D updrafts and the clouds containing them (Text S3 in Supporting Information S1) leads to similar conclusions. Most 3D updrafts are grid-scale, and 3D updraft width distributions are almost identical over land and ocean. Additionally, the horizontal distance from 3D updrafts to the edges of enclosing clouds follows a similar distribution over land and ocean, indicating a similar distribution of cloud widths in addition to a similar distribution of the widths of updraft cores.

We therefore conclude that neither land-ocean differences in updraft width, nor land-ocean differences in the widths of clouds that contain updrafts, are necessary to produce the simulated land-ocean contrast in updraft speeds in X-SHiELD.

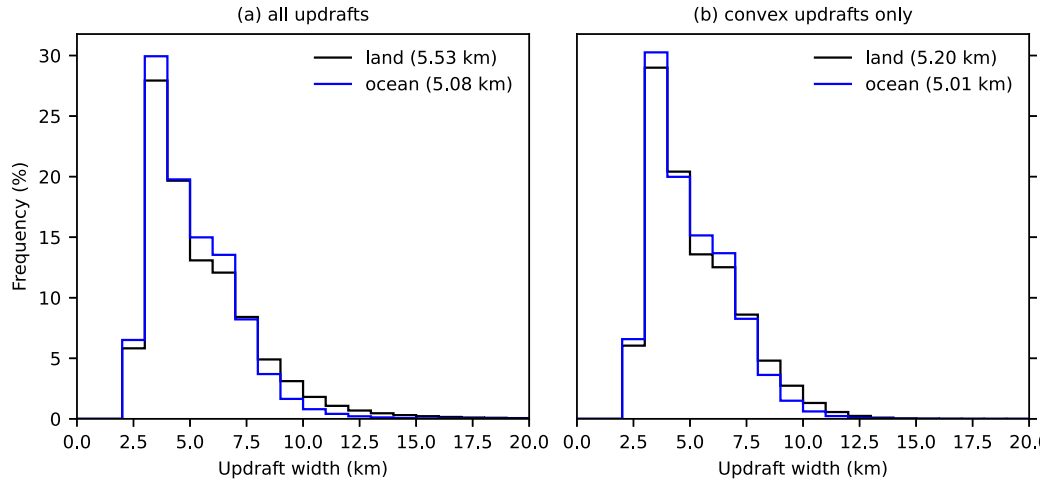

Figure 9. Distributions of low-level updraft widths in X-SHiELD with parameterized shallow convection disabled. Only updrafts within the tropical land and ocean regions defined in Section 2 are included. Distributions for updrafts over land and ocean are shown in black and blue, respectively. The distributions in panel (a) include all identified updrafts, and the distributions in panel (b) include only updrafts with convex cross-sections. Means for each distribution are shown in parentheses in panel legends.

5.3. Microphysics

Land-ocean differences in boundary layer aerosol concentrations and convective microphysics are a third hypothesized driver of the observed land-ocean contrast in convective intensity (e.g., E. Williams & Stanfill, 2002; E. Williams et al., 2002). Boundary layer aerosols are more abundant over land than ocean, and higher concentrations of cloud condensation nuclei produce higher cloud droplet number concentrations in warm clouds over land compared to ocean (e.g., Gryspeerdt et al., 2022). In turn, several hypothesized "aerosol invigoration" mechanisms link higher cloud droplet number concentrations to higher updraft buoyancy and more intense convection. Aerosol invigoration mechanisms rely either on the suppression of autoconversion in warm clouds, which can increase the latent heat released by condensate lofted through the freezing level (Rosenfeld et al., 2008) and increase environmental moistening by detrained condensate (Abbott & Cronin, 2021; Stevens & Feingold, 2009), or on reductions in supersaturation in warm clouds, which can increase the latent heat released by condensation (Fan et al., 2018).

Observations provide compelling evidence that aerosols may affect convective intensity. Observed cloud top heights often show positive correlations with aerosol optical depth or sub-cloud aerosol concentrations (e.g., Tao et al., 2012, and references therein). In the southeastern United States, midweek increases in summer afternoon thunderstorm activity coincide with midweek increases in near-surface aerosol concentrations (Bell et al., 2008, 2009). Observed lightning flash rates are elevated over shipping lanes in the Indian Ocean and South China Sea (Thornton et al., 2017), and simulations support the inference that this is linked to aerosol emissions from ships (Blossey et al., 2018). Controlling for the abundance of coarse sea spray aerosols—which can limit cloud droplet number concentrations over oceans even when fine aerosols are abundant—reveals strong positive correlations between reanalysis aerosol concentrations and observed proxies for convective intensity over both land and ocean (Pan et al., 2022). However, a number of recent studies have questioned both the generalizability of specific aerosol invigoration mechanisms and the soundness of the methods used to attribute invigoration to aerosols in observations (Igel & van den Heever, 2021; Kim et al., 2010; Öktem et al., 2023; Peters, Lebo, et al., 2023; Romps et al., 2023; A. C. Varble et al., 2023). In addition, determining whether aerosols are important drivers of the land-ocean contrast in convective intensity specifically is complicated by the fact that land-ocean differences in aerosol concentrations occur alongside land-ocean differences in (e.g.,) surface heat capacity, wetness, and heterogeneity; and by the fact that satellite proxies for intense convection (reflectivity, lightning) can be modulated by aerosols even if aerosols do not affect updraft speeds (E. Williams et al., 2002; A. C. Varble et al., 2023).

X-SHiELD uses a simple single-moment microphysics scheme, but does include some representation of land-ocean differences in aerosol concentrations. Specifically, it uses an autoconversion scheme following Manton

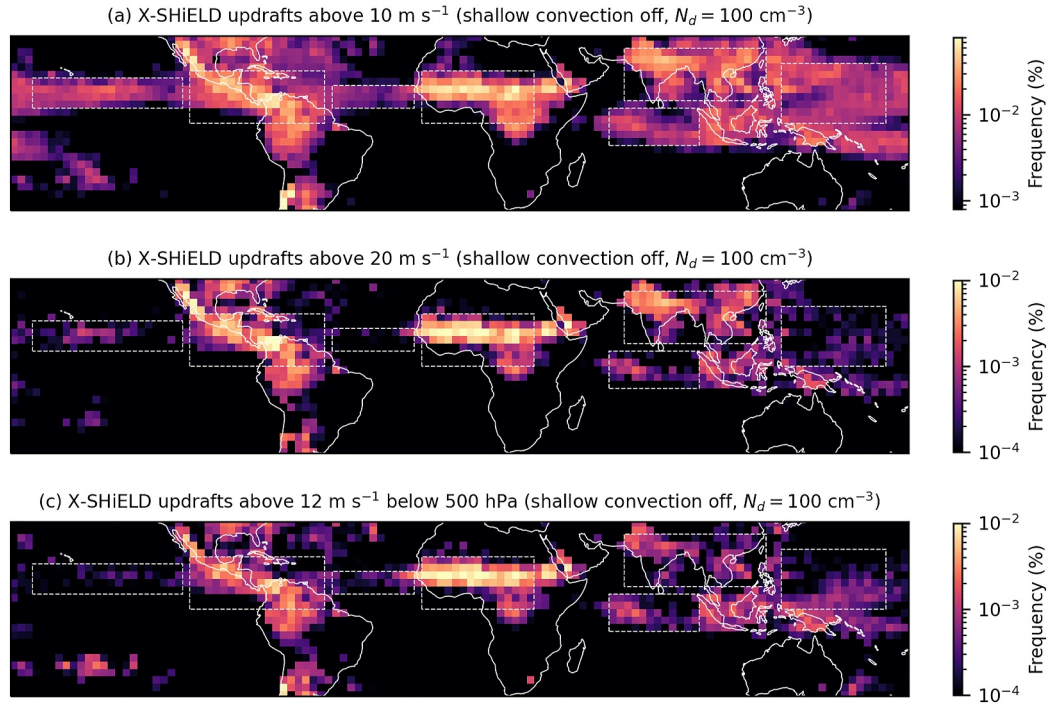

Figure 10. Frequency of column-maximum updraft velocities above 10 m s^{-1} (a) and 20 m s^{-1} (b), and frequency of updraft velocities above 12 m s^{-1} between the surface and 500 hPa (c), in X-SHiELD with parameterized shallow convection disabled and the cloud droplet number concentration N_d used by the autoconversion scheme set to 100 cm^{-3} over both land and ocean. Dashed lines show regions used to define the land-ocean contrast indices described in Section 2 and shown in Figure 2.

and Cotton (1977) that activates only when the mean cloud droplet radius—computed from the simulated liquid cloud mass concentration and a prescribed cloud droplet number concentration—exceeds a threshold radius of 8 μm (Zhou et al., 2022). In our default configuration, the prescribed cloud droplet number concentration is set to 100 cm^{-3} over ocean but 300 cm^{-3} over land. This raises the threshold cloud liquid mass concentration for autoconversion over land relative to ocean, and so might allow invigoration mechanisms that rely on the suppression of autoconversion in warm clouds to play a role in producing simulated land-ocean differences in updraft speeds. (Note that X-SHiELD uses saturation adjustment to treat phase changes between water vapor and cloud liquid, and so cannot model invigoration mechanisms that rely on changes in supersaturation in warm clouds).

To test whether microphysical differences play a role in the land-ocean contrast simulated by X-SHiELD, we rerun the simulation with parameterized shallow convection disabled, but set the cloud droplet number concentration used by the autoconversion scheme to 100 cm^{-3} over both land and ocean. Repeating our analysis of updraft speeds shows that this has essentially no impact on the frequency of strong updrafts, and in particular does not lead to a decrease in the frequency of strong updrafts over land in response to decreasing cloud droplet number concentrations (compare Figure 10 with Figure 5). This conclusion is reinforced by land-ocean contrast indices, which show little change in response to the reduction in cloud droplet number concentration over land (Figures 2b and 2c). We therefore conclude that land-ocean differences in convective microphysics are *not* necessary to produce the simulated land-ocean contrast in updraft speeds in X-SHiELD.

6. Summary and Discussion

We summarize our main results as follows:

- Observations contain greater than factor-of-10 differences in the frequency of proxies for intense convective updrafts, but only a small number of DYAMOND Summer simulations contain a factor-of-10 difference in the frequency of strong updrafts.

- In X-SHiELD, a GSRM developed at the Geophysical Fluid Dynamics Laboratory, the presence of a factor-of-10 land-ocean convective intensity contrast depends on whether the model is run with or without parameterized shallow convection.
- Three hypothesized drivers of the observed land-ocean contrast—land-ocean differences in CAPE, updraft width, and convective microphysics—can be ruled out as drivers of the simulated land-ocean contrast produced by X-SHiELD.

Stevens et al. (2019), in motivating the DYAMOND intercomparison project, argued that "an important next step in the application of [GSRMs] is to begin identifying which aspects of the simulated climate system are independent of the details of the GSRM implementation." Our results indicate that the strength of the land-ocean contrast in the intensity of deep convection is *not* independent of the details of GSRM implementations. This conclusion is supported by analysis of DYAMOND Summer simulations, which show considerable diversity in the strength of land-ocean differences in updraft speeds, and by experimentation with X-SHiELD, which reveals that the presence of a land-ocean contrast in updraft speeds can depend critically on the configuration of sub-grid-scale parameterizations. We suggest, instead, that a realistic land-ocean contrast be used as a *constraint* on GSRM development: it provides a way to assess GSRMs' ability to capture environmental controls on the intensity of deep convection in the present day, and therefore a way to build confidence in GSRMs' ability to project how patterns of extreme convective weather will evolve as climate change modifies the environments where convection occurs.

In addition, an increased focus on the land-ocean convective intensity contrast in GSRMs will yield tools for improving our understanding of the physical drivers of the observed land-ocean contrast. Our analysis of X-SHiELD simulations yielded negative results, in that we ruled out land-ocean differences in CAPE, updraft width, and microphysics as drivers of the simulated land-ocean contrast. This does not necessarily mean that land-ocean differences in CAPE, updraft width, or microphysics play no role in producing the land-ocean contrast seen in observations. X-SHiELD could be producing land-ocean differences in updraft speeds for the "wrong" reasons, and the absence of land-ocean differences in CAPE, updraft widths, or microphysics could plausibly explain why X-SHiELD's land-ocean contrast compares imperfectly with observations. Repeating our analysis in other GSRMs—particularly ones that, like X-SHiELD, can produce a clear land-ocean contrast—would help clarify whether our conclusions about drivers of land-ocean differences in updraft speeds are robust across GSRMs.

This work leaves several questions open as topics for future research. Perhaps most importantly: what physical process *does* drive the simulated land-ocean contrast in X-SHiELD? Our three negative results are consistent with Robinson et al. (2011), which rules out CAPE, boundary layer depth, and microphysics as important controls on land-ocean differences in convective intensity in short-duration limited-area simulations. Robinson et al. (2011) argues that the most likely driver in their simulations is mesoscale surface heterogeneity, which produces variations in surface thermal forcing that lead to more intense convection. We made the decision to focus on other possible drivers in this paper largely because the causal chain that might link surface heterogeneity to convective intensity has not, in our view, been articulated as clearly as causal chains that originate with CAPE, updraft width, and aerosols. Nevertheless, we view surface heterogeneity as a promising starting point for further exploration of the drivers of the simulated land-ocean contrast in X-SHiELD. Examining snapshots from the X-SHiELD simulation with parameterized shallow convection disabled (Figure 11) provides tentative evidence that surface heterogeneities contribute to local lifting over land but not ocean: lifting in the oceanic boundary layer occurs almost exclusively at the edges of convective cold pools, while boundary layer lifting over land occurs both on the margins of cold pools and in regions where no cold pools are present. Including realistic surface heterogeneity in simulations of convection over the Sahel (the land region shown in Figure 11) can increase the strength of mid-level convection (Mantsis et al., 2020); future GSRM studies could build on this result by examing how the intensity of deep convection changes in mechanism denial experiments that filter out mesoscale variability in surface properties over land. Finally, we note that the difficulty of accurately modeling boundary layer processes that link surface heterogeneity to deep convection in models with 3–4 km resolution could explain why most models in the DYAMOND ensemble struggle to produce a clear land-ocean contrast in convective intensity.

An alternative hypothesized driver that future work could explore is a land-ocean difference in the efficiency of rain formation, but driven by land-ocean differences in warm cloud depth rather than aerosol concentrations (e.g., Cecil et al., 2005). However, changes in warm cloud depth height do not appear to be a primary control on the strength of the land-ocean contrast simulated by X-SHiELD. The strength of the land-ocean contrast differs

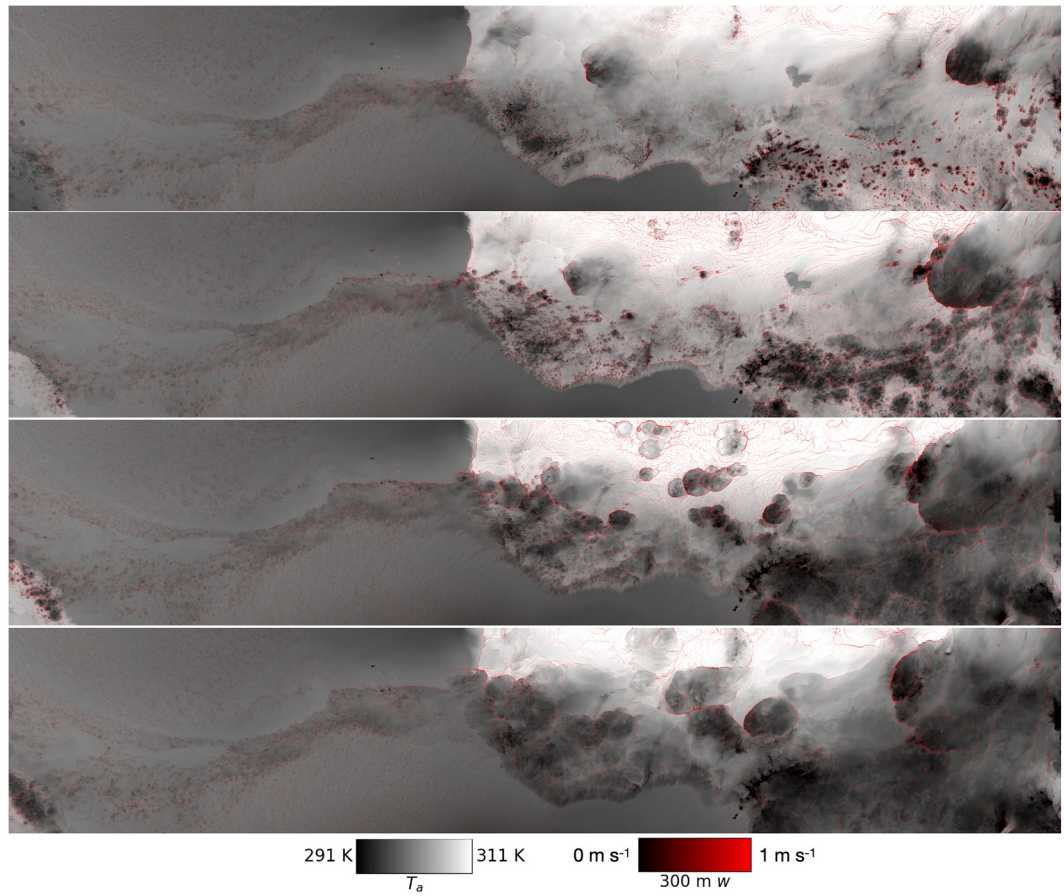

Figure 11. Surface air temperature and vertical velocity in the 7th model level (approximately 300 m above the surface) over the equatorial Atlantic and Sahel in four snapshots from the X-SHiELD simulation with parameterized shallow convection disabled. The dates and times of the snapshots are, from top to bottom, 11 August 2016 at 12Z, 15Z, 18Z, and 21Z. Full-resolution images with one pixel per model grid cell are available as supplementary data.

between simulations with parameterized shallow convection enabled and disabled primarily due to differences in the frequency of strong oceanic updrafts, but oceanic lifting condensation level (LCL) heights are less than 1 km in both simulations, meaning that both simulations produce deep warm cloud layers over ocean.

Land-ocean differences in mid-level relative humidity could potentially lead to land-ocean differences in convective intensity by influencing updraft dilution, but X-SHiELD does not produce systematic differences in mean relative humidity over land and ocean. In the simulation with parameterized shallow convection disabled, strong updrafts are much more common over western and central Africa than in the tropical western Pacific (Figure 5), but mean relative humidity is higher throughout the entire depth of the troposphere over the western Pacific (Figure S8 in Supporting Information S1). However, changes in convective organization can lead to differences in updraft dilution independent of changes in mean relative humidity (e.g., Wing & Cronin, 2016). Oceanic convection becomes noticeably less organized when parameterized shallow convection is disabled in X-SHiELD (Figure 6), and future work could explore whether this leads to a land-ocean difference in updraft dilution that can be linked to a land-ocean difference in convective organization.

A second unresolved question is why the X-SHiELD shallow convection scheme has such a dramatic effect on land-ocean differences in convective intensity. The scheme restricts the depth of the parameterized convective plume to no higher than the 700 hPa pressure level, which produces a peak in shallow convective heating at 700 hPa. We initially suspected that this might produce capping inversions over ocean that lead to buildup of high CAPE values, similar to continental regions that support particularly intense convection (Carlson et al., 1983; Houze Jr et al., 2007; Rasmussen & Houze, 2011). However, we were unable to find clear evidence linking the use of parameterized shallow convection to systematic increases in convective inhibition (a measure of the strength of

capping inversions) or CAPE over tropical oceans. We also confirmed that land-ocean differences in tuning parameters that affect triggering, rain formation, and rain evaporation in the shallow convection scheme—which are present in its default configuration—were not somehow responsible for suppressing the land-ocean contrast. Repeating the updraft width analysis described in Section 5.2 for the X-SHiELD simulation with parameterized convection enabled does reveal a slight shift toward wider low-level updrafts with shallow convection enabled (Figure S12 in Supporting Information S1). The shift is relatively small, so we are skeptical that it is responsible for the dramatic change in oceanic convective intensity, and its drivers remain unclear, but its importance could be assessed more carefully in future work. More generally, further experimentation with the X-SHiELD shallow convection scheme (e.g., by running simulations without a hard limit on the depth of the parameterized plume) might help clarify why the scheme has such a dramatic impact on the intensity of deep convection.

Although this paper focuses on differences in convective intensity between land and ocean broadly, GSRM development and our understanding of the physics of intense convection could both benefit from a more detailed evaluation of the geographic distribution of intense convection simulated by GSRMs. ICON (Figure 3m), UM (Figure 3r), and X-SHiELD with parameterized shallow convection disabled (Figure 5) produce a clear land-ocean contrast in the frequency of very strong updrafts, but comparing the distribution of simulated 20 m s^{-1} updrafts with the distribution of deep 40 dBZ echoes in observations (Figure 1) suggests that even these "good" models may produce too much intense convection in some regions (the Gulf of Mexico in ICON and the tropical western Pacific in ICON and UM) and too little in others (southern India in all three models and Indonesia in ICON and X-SHiELD). Understanding whether these biases are real will require a better understanding of the relationship between updraft speeds and observable proxies for intense convection, and could benefit from using observations of microwave brightness temperatures (e.g., E. J. Zipser, 2003; E. J. Zipser et al., 2006) as an additional satellite proxy with better sampling than GPM reflectivity profiles. Assuming the biases are real, they provide an additional target for improvement in future GSRM generations and an opportunity to refine our understanding of controls on the distribution of intense convection in nature.

A final overarching question, with potential ramifications beyond the specific problem of the land-ocean convective intensity contrast, is whether the ∼3 km resolution of GSRMs can adequately capture key properties of deep convection. Limited-area case studies with cloud-resolving simulations suggest that kilometer-scale models may significantly overestimate updraft velocities in deep convection (Fan et al., 2017; A. Varble et al., 2014), and idealized RCE simulations suggest that updraft widths and updraft velocities converge only at horizontal resolutions of ∼100 m (Jeevanjee, 2017). Could finer resolution produce a stronger simulated land-ocean contrast in the frequency of only moderately strong convection, perhaps by allowing simulations to capture land-ocean differences in updraft width that are impossible to resolve at 3 km resolution? Might this improve agreement with the land-ocean contrast seen in observations? These questions could be addressed by running X-SHiELD simulations on a nested grid, which permits extremely high resolution on a subset of the globe at reasonable computational expense (Mouallem et al., 2022). In addition to improving our understanding of controls on convective intensity, such simulations would provide a way to assess the robustness of resolution-sensitive and climate-relevant parameters like precipitation efficiency and anvil cloud fraction (Jeevanjee & Zhou, 2022; Lindzen et al., 2001; Mauritsen & Stevens, 2015; Sherwood et al., 2020; Zhao, 2014) in a frontier climate modeling tool.

Data Availability Statement

Public releases of X-SHiELD are available at https://github.com/NOAA-GFDL/SHiELD_build, and code for the version of X-SHiELD used in this paper is available in Harris et al. (2022). DYAMOND simulation outputs are archived by the German Climate Computing Center. TRMM lightning imaging sensor data is available in Albrecht et al. (2016a), GPM 2ADPR data is available in Iguchi and Meneghini (2021), and NOAA GSOD records are available in NOAA National Centers of Environmental Information (1999). Modifications to the X-SHiELD source code, X-SHiELD input files, processed data, and analysis scripts are available at Abbott et al. (2025).

Acknowledgments
This research was supported by a grant from the Earth's Radiation Budget Initiative, NOAA CPO Climate & CI (Grant 03-01-07-001). This report was prepared by the authors under award NA18OAR4320123 from the National Oceanic and Atmospheric Administration, U.S. Department of Commerce. The authors thank Pu Lin, Leo Donner, and three anonymous reviewers for thoughtful reviews. DYAMOND data management was provided by the German Climate Computing Center (DKRZ) and supported through the projects ESiWACE and ESiWACE2. The projects ESiWACE and ESiWACE2 have received funding from the European Union's Horizon 2020 research and innovation programme under Grant agreements No 675191 and 823988. This work used resources of the Deutsches Klimarechenzentrum (DKRZ) granted by its Scientific Steering Committee (WLA) under project IDs bk1040 and bb1153.

References

Abbott, T. H., & Cronin, T. W. (2021). Aerosol invigoration of atmospheric convection through increases in humidity. *Science*, *371*(6524), 83–85. https://doi.org/10.1126/science.abc5181

Abbott, T. H., Jeevanjee, N., Cheng, K.-Y., Zhou, L., & Harris, L. (2025). Data for "the land-ocean contrast in deep convective intensity in a global storm-resolving model" [Dataset]. *Harvard Dataverse*. https://doi.org/10.7910/DVN/JHYEQI

Albrecht, R. I., Goodman, S. J., Buechler, D. E., Blakeslee, R. J., & Christian, H. J. (2016a). LIS 0.1 degree very high resolution gridded lightning climatology data collection [Dataset]. Data Sets. Available Online. https://doi.org/10.5067/LIS/LIS/DATA306

Albrecht, R. I., Goodman, S. J., Buechler, D. E., Blakeslee, R. J., & Christian, H. J. (2016b). Where are the lightning hotspots on earth? *Bulletin of the American Meteorological Society*, *97*(11), 2051–2068. https://doi.org/10.1175/bams-d-14-00193.1

Arakawa, A., & Schubert, W. H. (1974). Interaction of a cumulus cloud ensemble with the large-scale environment, part I. *Journal of the Atmospheric Sciences*, *31*(3), 674–701. https://doi.org/10.1175/1520-0469(1974)031<0674:ioacce>2.0.co;2

Bang, S. D., & Zipser, E. J. (2015). Differences in size spectra of electrified storms over land and ocean. *Geophysical Research Letters*, *42*(16), 6844–6851. https://doi.org/10.1002/2015gl065264

Barlage, M., Zeng, X., Wei, H., & Mitchell, K. E. (2005). A global 0.05° maximum albedo dataset of snow-covered land based on Modis observations. *Geophysical Research Letters*, *32*(17). https://doi.org/10.1029/2005gl022881

Bell, T. L., Rosenfeld, D., & Kim, K.-M. (2009). Weekly cycle of lightning: Evidence of storm invigoration by pollution. *Geophysical Research Letters*, *36*(23). https://doi.org/10.1029/2009gl040915

Bell, T. L., Rosenfeld, D., Kim, K.-M., Yoo, J.-M., Lee, M.-I., & Hahnenberger, M. (2008). Midweek increase in us summer rain and storm heights suggests air pollution invigorates rainstorms. *Journal of Geophysical Research*, *113*(D2). https://doi.org/10.1029/2007jd008623

Blanchard, D. O. (1998). Assessing the vertical distribution of convective available potential energy. *Weather and Forecasting*, *13*(3), 870–877. https://doi.org/10.1175/1520-0434(1998)013<0870:atvdoc>2.0.co;2

Blossey, P. N., Bretherton, C. S., Thornton, J. A., & Virts, K. S. (2018). Locally enhanced aerosols over a shipping lane produce convective invigoration but weak overall indirect effects in cloud-resolving simulations. *Geophysical Research Letters*, *45*(17), 9305–9313. https://doi.org/10.1029/2018gl078682

Byers, H. R., & Braham, R. R. (1949). *The thunderstorm: Report of the thunderstorm project*. US Government Printing Office.

Carlson, T., Benjamin, S., Forbes, G., & Li, Y. (1983). Elevated mixed layers in the regional severe storm environment: Conceptual model and case studies. *Monthly Weather Review*, *111*(7), 1453–1474. https://doi.org/10.1175/1520-0493(1983)111<1453:emlitr>2.0.co;2

Cecil, D. J., Buechler, D. E., & Blakeslee, R. J. (2014). Gridded lightning climatology from TRMM-LIS and OTD: Dataset description. *Atmospheric Research*, *135*, 404–414. https://doi.org/10.1016/j.atmosres.2012.06.028

Cecil, D. J., Goodman, S. J., Boccippio, D. J., Zipser, E. J., & Nesbitt, S. W. (2005). Three years of TRMM precipitation features. Part I: Radar, radiometric, and lightning characteristics. *Monthly Weather Review*, *133*(3), 543–566. https://doi.org/10.1175/mwr-2876.1

Charney, J. G. (1947). The dynamics of long waves in a Baroclinic westerly current. *Journal of the Atmospheric Sciences*, *4*(5), 136–162. https://doi.org/10.1175/1520-0469(1947)004⟨0136:TDOLWI⟩2.0.CO;2

Christian, H. J., Blakeslee, R. J., Boccippio, D. J., Boeck, W. L., Buechler, D. E., Driscoll, K. T., et al. (2003). Global frequency and distribution of lightning as observed from space by the optical transient detector. *Journal of Geophysical Research*, *108*(D1), ACL4. https://doi.org/10.1029/2002jd002347

Danielson, J. J., & Gesch, D. B. (2011). *Global Multi-Resolution Terrain Elevation Data 2010 (GMTED2010)*. (Tech. Rep.). US Geological Survey.

Drager, A. J., Grant, L. D., & van den Heever, S. C. (2020). Cold pool responses to changes in soil moisture. *Journal of Advances in Modeling Earth Systems*, *12*(8), e2019MS001922. https://doi.org/10.1029/2019ms001922

Ek, M., Mitchell, K., Lin, Y., Rogers, E., Grunmann, P., Koren, V., et al. (2003). Implementation of Noah land surface model advances in the National Centers for Environmental Prediction operational mesoscale Eta model. *Journal of Geophysical Research*, *108*(D22). https://doi.org/10.1029/2002jd003296

Emanuel, K. (2007). Quasi-equilibrium dynamics of the tropical atmosphere. *The global circulation of the atmosphere*, *186*, 218.

Emanuel, K. (2023). On the physics of high CAPE. *Journal of the Atmospheric Sciences*, *80*(11), 2669–2683. https://doi.org/10.1175/jas-d-23-0060.1

Fan, J., Han, B., Varble, A., Morrison, H., North, K., Kollias, P., et al. (2017). Cloud-resolving model intercomparison of an MC3E squall line case: Part I—Convective updrafts. *Journal of Geophysical Research: Atmospheres*, *122*(17), 9351–9378. https://doi.org/10.1002/2017jd026622

Fan, J., Rosenfeld, D., Zhang, Y., Giangrande, S. E., Li, Z., Machado, L. A., et al. (2018). Substantial convection and precipitation enhancements by ultrafine aerosol particles. *Science*, *359*(6374), 411–418. https://doi.org/10.1126/science.aan8461

Galway, J. G. (1956). The lifted index as a predictor of latent instability. *Bulletin of the American Meteorological Society*, *37*(10), 528–529. https://doi.org/10.1175/1520-0477-37.10.528

Gao, F., Schaaf, C. B., Strahler, A. H., Roesch, A., Lucht, W., & Dickinson, R. (2005). Modis bidirectional reflectance distribution function and albedo climate modeling grid products and the variability of albedo for major global vegetation types. *Journal of Geophysical Research*, *110*(D1). https://doi.org/10.1029/2004jd005190

Gryspeerdt, E., McCoy, D. T., Crosbie, E., Moore, R. H., Nott, G. J., Painemal, D., et al. (2022). The impact of sampling strategy on the cloud droplet number concentration estimated from satellite data. *Atmospheric Measurement Techniques*, *15*(12), 3875–3892. https://doi.org/10.5194/amt-15-3875-2022

Hallett, J., Sax, R. I., Lamb, D., & Murty, A. R. (1978). Aircraft measurements of ice in Florida Cumuli. *Quarterly Journal of the Royal Meteorological Society*, *104*(441), 631–651. https://doi.org/10.1256/smsqj.44107

Han, J., & Bretherton, C. S. (2019). TKE-based moist Eddy-Diffusivity Mass-Flux (EDMF) parameterization for vertical turbulent mixing. *Weather and Forecasting*, *34*(4), 869–886. https://doi.org/10.1175/waf-d-18-0146.1

Han, J., Wang, W., Kwon, Y. C., Hong, S.-Y., Tallapragada, V., & Yang, F. (2017). Updates in the NCEP GFS cumulus convection schemes with scale and aerosol awareness. *Weather and Forecasting*, *32*(5), 2005–2017. https://doi.org/10.1175/waf-d-17-0046.1

Hansen, Z. R., & Back, L. E. (2015). Higher surface Bowen ratios ineffective at increasing updraft intensity. *Geophysical Research Letters*, *42*(23), 10–503. https://doi.org/10.1002/2015gl066878

Hansen, Z. R., Back, L. E., & Zhou, P. (2020). Boundary layer Quasi-equilibrium limits convective intensity enhancement from the diurnal cycle in surface heating. *Journal of the Atmospheric Sciences*, *77*(1), 217–237. https://doi.org/10.1175/jas-d-18-0346.1

Harris, L., Chen, X., Putnam, W., Zhou, L., & Chen, J.-H. (2021). A scientific description of the GFDL finite-volume cubed-sphere dynamical core. https://doi.org/10.25923/6nhs-5897

Harris, L., Zhou, L., Chen, J.-H., Gao, K., Tong, M., Cheng, K.-Y., & Clark, S. (2022). Shield PIRE_production_202103 [Dataset]. *Zenodo*. https://doi.org/10.5281/zenodo.6941033

Harris, L., Zhou, L., Lin, S.-J., Chen, J.-H., Chen, X., Gao, K., et al. (2020). GFDL SHiELD: A unified system for weather-to-seasonal prediction. *Journal of Advances in Modeling Earth Systems*, *12*(10), e2020MS002223. https://doi.org/10.1029/2020ms002223

Heymsfield, G. M., Tian, L., Heymsfield, A. J., Li, L., & Guimond, S. (2010). Characteristics of deep tropical and subtropical convection from nadir-viewing high-altitude airborne Doppler radar. *Journal of the Atmospheric Sciences*, *67*(2), 285–308. https://doi.org/10.1175/2009jas3132.1

Heymsfield, G. M., Tian, L., Li, L., McLinden, M., & Cervantes, J. I. (2013). Airborne radar observations of severe hailstorms: Implications for future spaceborne radar. *Journal of Applied Meteorology and Climatology*, *52*(8), 1851–1867. https://doi.org/10.1175/jamc-d-12-0144.1

Houze, R. A., Jr., Rasmussen, K. L., Zuluaga, M. D., & Brodzik, S. R. (2015). The variable nature of convection in the tropics and subtropics: A legacy of 16 years of the tropical rainfall measuring mission satellite. *Reviews of Geophysics*, *53*(3), 994–1021. https://doi.org/10.1002/2015rg000488

Houze, R. A., Jr., Wilton, D. C., & Smull, B. F. (2007). Monsoon convection in the Himalayan region as seen by the TRMM precipitation radar. *Quarterly Journal of the Royal Meteorological Society*, *133*(627), 1389–1411. https://doi.org/10.1002/qj.106

Igel, A. L., & van den Heever, S. C. (2021). Invigoration or enervation of convective clouds by aerosols? *Geophysical Research Letters*, *48*(16), e2021GL093804. https://doi.org/10.1029/2021gl093804

Iguchi, T., & Meneghini, R. (2021). GPM DPR precipitation profile L2A 1.5 hours 5 km v07 [Dataset]. *Goddard EARTH SCIENCES DATA and Information Services Center (GES DISC)*. https://doi.org/10.5067/GPM/DPR/GPM/2A/07

Jeevanjee, N. (2017). Vertical velocity in the gray zone. *Journal of Advances in Modeling Earth Systems*, *9*(6), 2304–2316. https://doi.org/10.1002/2017ms001059

Jeevanjee, N., & Zhou, L. (2022). On the resolution-dependence of anvil cloud fraction and precipitation efficiency in radiative-convective equilibrium. *Journal of Advances in Modeling Earth Systems*, *14*(3), 1–17. https://doi.org/10.1029/2021ms002759

Jorgensen, D. P., & LeMone, M. A. (1989). Vertical velocity characteristics of oceanic convection. *Journal of the Atmospheric Sciences*, *46*(5), 621–640. https://doi.org/10.1175/1520-0469(1989)046<0621:vvcooc>2.0.co;2

Kim, K.-Y., Park, R. J., Kim, K.-R., & Na, H. (2010). Weekend effect: Anthropogenic or natural? *Geophysical Research Letters*, *37*(9). https://doi.org/10.1029/2010gl043233

Lawson, R. P., Woods, S., & Morrison, H. (2015). The microphysics of ice and precipitation development in tropical cumulus clouds. *Journal of the Atmospheric Sciences*, *72*(6), 2429–2445. https://doi.org/10.1175/jas-d-14-0274.1

LeMone, M. A., & Zipser, E. J. (1980). Cumulonimbus vertical velocity events in GATE. Part I: Diameter, intensity and mass flux. *Journal of the Atmospheric Sciences*, *37*(11), 2444–2457. https://doi.org/10.1175/1520-0469(1980)037<2444:cvveig>2.0.co;2

Lindzen, R. S., Chou, M.-D., & Hou, A. Y. (2001). Does the earth have an adaptive infrared iris? *Bulletin of the American Meteorological Society*, *82*(3), 417–432. https://doi.org/10.1175/1520-0477(2001)082<0417:dtehaa>2.3.co;2

Liu, C., Cecil, D. J., Zipser, E. J., Kronfeld, K., & Robertson, R. (2012). Relationships between lightning flash rates and radar reflectivity vertical structures in thunderstorms over the tropics and subtropics. *Journal of Geophysical Research*, *117*(D6). https://doi.org/10.1029/2011jd017123

Liu, C., & Zipser, E. J. (2005). Global distribution of convection penetrating the tropical tropopause. *Journal of Geophysical Research*, *110*(D23). https://doi.org/10.1029/2005jd006063

Liu, C., & Zipser, E. J. (2015). The global distribution of largest, deepest, and most intense precipitation systems. *Geophysical Research Letters*, *42*(9), 3591–3595. https://doi.org/10.1002/2015gl063776

Liu, C., Zipser, E. J., Cecil, D. J., Nesbitt, S. W., & Sherwood, S. (2008). A cloud and precipitation feature database from nine years of TRMM observations. *Journal of Applied Meteorology and Climatology*, *47*(10), 2712–2728. https://doi.org/10.1175/2008jamc1890.1

Liu, S., Sindhu, K. D., & Kirshbaum, D. J. (2023). Observations of boundary layer convergence lines and associated updrafts in the us Southern great Plains. *Journal of the Atmospheric Sciences*, *80*(12), 2947–2968. https://doi.org/10.1175/jas-d-23-0089.1

Lucas, C., Zipser, E. J., & LeMone, M. A. (1994a). Convective available potential energy in the environment of oceanic and continental clouds: Correction and comments. *Journal of the Atmospheric Sciences*, *51*(24), 3829–3830. https://doi.org/10.1175/1520-0469(1994)051<3829:capeit>2.0.co;2

Lucas, C., Zipser, E. J., & Lemone, M. A. (1994b). Vertical velocity in oceanic convection off tropical Australia. *Journal of the Atmospheric Sciences*, *51*(21), 3183–3193. https://doi.org/10.1175/1520-0469(1994)051<3183:vvioco>2.0.co;2

Ma, H.-Y., Klein, S. A., Lee, J., Ahn, M.-S., Tao, C., & Gleckler, P. J. (2022). Superior daily and sub-daily precipitation statistics for intense and long-lived storms in global storm-resolving models. *Geophysical Research Letters*, *49*(8), e2021GL096759. https://doi.org/10.1029/2021gl096759

Manton, M. J., & Cotton, W. R. (1977). *Formulation of approximate equations for modeling moist deep convection on the mesoscale (No. 266)*. Department of Atmospheric Science, Colorado State University.

Mantsis, D. F., Sherwood, S., Dixit, V., Morrison, H., & Thompson, G. (2020). Mid-level clouds over the Sahara in a convection-permitting regional model. *Climate Dynamics*, *54*(7–8), 3425–3439. https://doi.org/10.1007/s00382-020-05188-4

Matsui, T., Chern, J.-D., Tao, W.-K., Lang, S., Satoh, M., Hashino, T., & Kubota, T. (2016). On the land–ocean contrast of tropical convection and microphysics statistics derived from TRMM satellite signals and global storm-resolving models. *Journal of Hydrometeorology*, *17*(5), 1425–1445. https://doi.org/10.1175/jhm-d-15-0111.1

Mauritsen, T., & Stevens, B. (2015). Missing iris effect as a possible cause of muted hydrological change and high climate sensitivity in models. *Nature Geoscience*, *8*(5), 346–351. https://doi.org/10.1038/ngeo2414

Mouallem, J., Harris, L., & Benson, R. (2022). Multiple same-level and telescoping nesting in GFDL's dynamical core. *Geoscientific Model Development*, *15*(11), 4355–4371. https://doi.org/10.5194/gmd-15-4355-2022

Mulholland, J., Peters, J., & Morrison, H. (2021). How does LCL height influence deep convective updraft width? *Geophysical Research Letters*, *48*(13), e2021GL093316. https://doi.org/10.1029/2021gl093316

Musil, D. J., Christopher, S. A., Deola, R. A., & Smith, P. L. (1991). Some interior observations of southeastern Montana hailstorms. *Journal of Applied Meteorology and Climatology*, *30*(12), 1596–1612. https://doi.org/10.1175/1520-0450(1991)030<1596:sioosm>2.0.co;2

Nesbitt, S. W., Cifelli, R., & Rutledge, S. A. (2006). Storm morphology and rainfall characteristics of TRMM precipitation features. *Monthly Weather Review*, *134*(10), 2702–2721. https://doi.org/10.1175/mwr3200.1

NOAA National Centers of Environmental Information. (1999). Global surface summary of the day—GSOD 1.0 [Dataset]. *NOAA National Centers for Environmental Information*.

Öktem, R., Romps, D. M., & Varble, A. C. (2023). No warm-phase invigoration of convection detected during Goamazon. *Journal of the Atmospheric Sciences*, *80*(10), 2345–2364. https://doi.org/10.1175/jas-d-22-0241.1

Palmer, T., & Stevens, B. (2019). The scientific challenge of understanding and estimating climate change. *Proceedings of the National Academy of Sciences*, *116*(49), 24390–24395. https://doi.org/10.1073/pnas.1906691116

Pan, Z., Mao, F., Rosenfeld, D., Zhu, Y., Zang, L., Lu, X., et al. (2022). Coarse sea spray inhibits lightning. *Nature Communications*, *13*(1), 4289. https://doi.org/10.1038/s41467-022-31714-5

Peters, J. M., Chavas, D. R., Su, C.-Y., Morrison, H., & Coffer, B. E. (2023a). An analytic formula for entraining cape in midlatitude storm environments. *Journal of the Atmospheric Sciences*, *80*(9), 2165–2186. https://doi.org/10.1175/jas-d-23-0003.1

Peters, J. M., Lebo, Z. J., Chavas, D. R., & Su, C.-Y. (2023b). Entrainment makes pollution more likely to weaken deep convective updrafts than invigorate them. *Geophysical Research Letters*, *50*(12), e2023GL103314. https://doi.org/10.1029/2023gl103314

Pollard, R. T., Rhines, P. B., & Thompson, R. O. (1973). The deepening of the wind-mixed layer. *Geophysical Fluid Dynamics*, *4*(4), 381–404. https://doi.org/10.1080/03091927208236105

Putman, W. M., & Lin, S.-J. (2007). Finite-volume transport on various cubed-sphere grids. *Journal of Computational Physics*, *227*(1), 55–78. https://doi.org/10.1016/j.jcp.2007.07.022

Rasmussen, K. L., & Houze, R. A. (2011). Orogenic convection in subtropical South America as seen by the TRMM satellite. *Monthly Weather Review*, *139*(8), 2399–2420. https://doi.org/10.1175/mwr-d-10-05006.1

Robinson, F., Sherwood, S., Gerstle, D., Liu, C., & Kirshbaum, D. J. (2011). Exploring the land–ocean contrast in convective vigor using islands. *Journal of the Atmospheric Sciences*, *68*(3), 602–618. https://doi.org/10.1175/2010jas3558.1

Romps, D. M., Charn, A. B., Holzworth, R. H., Lawrence, W. E., Molinari, J., & Vollaro, D. (2018). CAPE times P explains lightning over land but not the land-ocean contrast. *Geophysical Research Letters*, *45*(22), 12–623. https://doi.org/10.1029/2018gl080267

Romps, D. M., Latimer, K., Zhu, Q., Jurkat-Witschas, T., Mahnke, C., Prabhakaran, T., et al. (2023). Air pollution unable to intensify storms via warm-phase invigoration. *Geophysical Research Letters*, *50*(2), e2022GL100409. https://doi.org/10.1029/2022gl100409

Romps, D. M., Seeley, J. T., Vollaro, D., & Molinari, J. (2014). Projected increase in lightning strikes in the United States due to global warming. *Science*, *346*(6211), 851–854. https://doi.org/10.1126/science.1259100

Rosenfeld, D., Lohmann, U., Raga, G. B., O'Dowd, C. D., Kulmala, M., Fuzzi, S., et al. (2008). Flood or drought: How do aerosols affect precipitation? *Science*, *321*(5894), 1309–1313. https://doi.org/10.1126/science.1160606

Rutledge, S. A., Williams, E. R., & Keenan, T. D. (1992). The down under Doppler and Electricity Experiment (DUNDEE): Overview and preliminary results. *Bulletin of the American Meteorological Society*, *73*(1), 3–16. https://doi.org/10.1175/1520-0477(1992)073<0003:tdudae>2.0.co;2

Sarbeng, E. (2023). *Intense tropical thunderstorms in a future warmer climate*. (Doctoral Dissertation). Monash University. https://doi.org/10.26180/23118494.v1

Schaaf, C. B., Gao, F., Strahler, A. H., Lucht, W., Li, X., Tsang, T., et al. (2002). First operational BRDF, albedo nadir reflectance products from Modis. *Remote Sensing of Environment*, *83*(1–2), 135–148. https://doi.org/10.1016/s0034-4257(02)00091-3

Seeley, J. T., & Romps, D. M. (2016). Tropical cloud buoyancy is the same in a world with or without ice. *Geophysical Research Letters*, *43*(7), 3572–3579. https://doi.org/10.1002/2016gl068583

Sherwood, S. C., Webb, M. J., Annan, J. D., Armour, K. C., Forster, P. M., Hargreaves, J. C., et al. (2020). An assessment of earth's climate sensitivity using multiple lines of evidence. *Reviews of Geophysics*, *58*(4), e2019RG000678. https://doi.org/10.1029/2019rg000678

Sobel, A. H., & Bretherton, C. S. (2000). Modeling tropical precipitation in a single column. *Journal of Climate*, *13*(24), 4378–4392. https://doi.org/10.1175/1520-0442(2000)013<4378:mtpias>2.0.co;2

Stevens, B., Acquistapace, C., Hansen, A., Heinze, R., Klinger, C., Klocke, D., et al. (2020). The added value of large-eddy and storm-resolving models for simulating clouds and precipitation. *Journal of the Meteorological Society of Japan. Ser. II*, *98*(2), 395–435. https://doi.org/10.2151/jmsj.2020-021

Stevens, B., & Feingold, G. (2009). Untangling aerosol effects on clouds and precipitation in a buffered system. *Nature*, *461*(7264), 607–613. https://doi.org/10.1038/nature08281

Stevens, B., Satoh, M., Auger, L., Biercamp, J., Bretherton, C. S., Chen, X., et al. (2019). DYAMOND: The DYnamics of the atmospheric general circulation modeled on non-hydrostatic domains. *Progress in Earth and Planetary Science*, *6*(1), 1–17. https://doi.org/10.1186/s40645-019-0304-z

Takahashi, H., Luo, Z. J., & Stephens, G. (2021). Revisiting the entrainment relationship of convective plumes: A perspective from global observations. *Geophysical Research Letters*, *48*(6), e2020GL092349. https://doi.org/10.1029/2020gl092349

Takahashi, H., Luo, Z. J., Stephens, G., & Mulholland, J. P. (2023). Revisiting the land-ocean contrasts in deep convective cloud intensity using global satellite observations. *Geophysical Research Letters*, *50*(5), e2022GL102089. https://doi.org/10.1029/2022gl102089

Takahashi, T. (1978). Riming electrification as a charge generation mechanism in thunderstorms. *Journal of the Atmospheric Sciences*, *35*(8), 1536–1548. https://doi.org/10.1175/1520-0469(1978)035<1536:reaacg>2.0.co;2

Tao, W.-K., Chen, J.-P., Li, Z., Wang, C., & Zhang, C. (2012). Impact of aerosols on convective clouds and precipitation. *Reviews of Geophysics*, *50*(2). https://doi.org/10.1029/2011rg000369

Thornton, J. A., Virts, K. S., Holzworth, R. H., & Mitchell, T. P. (2017). Lightning enhancement over major oceanic shipping lanes. *Geophysical Research Letters*, *44*(17), 9102–9111. https://doi.org/10.1002/2017gl074982

Tuckman, P., Agard, V., & Emanuel, K. (2023). Evolution of convective energy and inhibition before instances of large CAPE. *Monthly Weather Review*, *151*(1), 321–338. https://doi.org/10.1175/mwr-d-21-0302.1

Varble, A., Zipser, E. J., Fridlind, A. M., Zhu, P., Ackerman, A. S., Chaboureau, J.-P., et al. (2014). Evaluation of cloud-resolving and limited area model intercomparison simulations using TWP-ICE observations: 1. Deep convective updraft properties. *Journal of Geophysical Research: Atmospheres*, *119*(24), 13–891. https://doi.org/10.1002/2013jd021371

Varble, A. C., Igel, A. L., Morrison, H., Grabowski, W. W., & Lebo, Z. J. (2023). Opinion: A critical evaluation of the evidence for aerosol invigoration of deep convection. *Atmospheric Chemistry and Physics*, *23*(21), 13791–13808. https://doi.org/10.5194/acp-23-13791-2023

Wang, Z., Franke, J. A., Luo, Z., & Moyer, E. J. (2021). Reanalyses and a high-resolution model fail to capture the "high tail" of CAPE distributions. *Journal of Climate*, *34*(21), 8699–8715. https://doi.org/10.1175/jcli-d-20-0278.1

Webster, P. J., & Houze Jr, R. A. (1991). The Equatorial Mesoscale Experiment (EMEX): An overview. *Bulletin of the American Meteorological Society*, *72*(10), 1481–1506. https://doi.org/10.1175/1520-0477(1991)072<1481:temeao>2.0.co;2

Williams, E., Mushtak, V., Rosenfeld, D., Goodman, S., & Boccippio, D. (2005). Thermodynamic conditions favorable to superlative thunderstorm updraft, mixed phase microphysics and lightning flash rate. *Atmospheric Research*, *76*(1–4), 288–306. https://doi.org/10.1016/j.atmosres.2004.11.009

Williams, E., Rosenfeld, D., Madden, N., Gerlach, J., Gears, N., Atkinson, L., et al. (2002). Contrasting convective regimes over the Amazon: Implications for cloud electrification. *Journal of Geophysical Research*, *107*(D20), LBA50. https://doi.org/10.1029/2001jd000380

Williams, E., & Stanfill, S. (2002). The physical origin of the land–ocean contrast in lightning activity. *Comptes Rendus Physique*, *3*(10), 1277–1292. https://doi.org/10.1016/s1631-0705(02)01407-x

Williams, E. R., Geotis, S., Renno, N., Rutledge, S., Rasmussen, E., & Rickenbach, T. (1992). A radar and electrical study of tropical "hot towers". *Journal of the Atmospheric Sciences*, *49*(15), 1386–1395. https://doi.org/10.1175/1520-0469(1992)049<1386:araeso>2.0.co;2

Wing, A. A., & Cronin, T. W. (2016). Self-aggregation of convection in long channel geometry. *Quarterly Journal of the Royal Meteorological Society*, *142*(694), 1–15. https://doi.org/10.1002/qj.2628

Wood, N., Staniforth, A., White, A., Allen, T., Diamantakis, M., Gross, M., et al. (2014). An inherently mass-conserving semi-implicit semi-Lagrangian discretization of the deep-atmosphere global non-hydrostatic equations. *Quarterly Journal of the Royal Meteorological Society*, *140*(682), 1505–1520. https://doi.org/10.1002/qj.2235

Zängl, G., Reinert, D., Rípodas, P., & Baldauf, M. (2015). The ICON (ICOsahedral Non-hydrostatic) modelling framework of DWD and MPI-M: Description of the non-hydrostatic dynamical core. *Quarterly Journal of the Royal Meteorological Society*, *141*(687), 563–579. https://doi.org/10.1002/qj.2378

Zhang, Y., & Fueglistaler, S. (2020). How tropical convection couples high moist static energy over land and ocean. *Geophysical Research Letters*, *47*(2), 1–8. https://doi.org/10.1029/2019gl086387

Zhao, M. (2014). An investigation of the connections among convection, clouds, and climate sensitivity in a global climate model. *Journal of Climate*, *27*(5), 1845–1862. https://doi.org/10.1175/jcli-d-13-00145.1

Zhou, L., Harris, L., Chen, J.-H., Gao, K., Guo, H., Xiang, B., et al. (2022). Improving global weather prediction in GFDL SHiELD through an upgraded GFDL cloud microphysics scheme. *Journal of Advances in Modeling Earth Systems*, *14*(7), e2021MS002971. https://doi.org/10.1029/2021ms002971

Zipser, E., & LeMone, M. (1980). Cumulonimbus vertical velocity events in GATE. Part II: Synthesis and model core structure. *Journal of the Atmospheric Sciences*, *37*(11), 2458–2469. https://doi.org/10.1175/1520-0469(1980)037<2458:cvveig>2.0.co;2

Zipser, E. J. (2003). Some views on "hot towers" after 50 years of tropical field programs and two years of TRMM data. *Meteorological Monographs*, *29*(51), 49–58. https://doi.org/10.1175/0065-9401(2003)029<0049:csvoht>2.0.co;2

Zipser, E. J., Cecil, D. J., Liu, C., Nesbitt, S. W., & Yorty, D. P. (2006). Where are the most intense thunderstorms on earth? *Bulletin of the American Meteorological Society*, *87*(8), 1057–1072. https://doi.org/10.1175/bams-87-8-1057

Zipser, E. J., & Lutz, K. R. (1994). The vertical profile of radar reflectivity of convective cells: A strong indicator of storm intensity and lightning probability? *Monthly Weather Review*, *122*(8), 1751–1759. https://doi.org/10.1175/1520-0493(1994)122<1751:tvporr>2.0.co;2